Ocean Modelling 201 (2026) 102702

Contents lists available at ScienceDirect

Ocean Modelling

journal homepage: www.elsevier.com/locate/ocemod

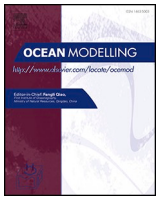

Impact of intertidal habitats on storm-induced flooding in estuaries: Application to the Thames Estuary, UK

Renjie Zhu [a,b,c,d], Wei Zhang [a,b,c], Xiaoyan Wei [d,*]

[a] State Key Laboratory of Water Disaster Prevention, Hohai University, Nanjing, China
[b] Key Laboratory of Ministry of Education for Coastal Disaster and Protection, Hohai University, Nanjing, China
[c] College of Harbour, Coastal and Offshore Engineering, Hohai University, Nanjing, China
[d] National Oceanography Centre, Liverpool, United Kingdom

ARTICLE INFO

Keywords:
Intertidal habitats
Storm-induced flooding
Semi-analytical model
Nature-based solution
Thames Estuary
Xaver

ABSTRACT

Intertidal habitats have been rapidly reduced worldwide due to land reclamation. To mitigate risks related to flooding, erosion, and biodiversity loss, intertidal restoration and creation are increasingly implemented worldwide. Nevertheless, the mechanisms through which these habitats affect estuarine flooding are still underexplored. This study developed a three-dimensional, idealized semi-analytical model to systematically examine intertidal effects on extreme high water levels (EWL) in estuaries. As a case study, the model was applied to the idealized Thames Estuary (UK) during the storm Xaver, the strongest North Sea surge in the last seven decades. Our results show that semi-diurnal tides and lower-frequency surges (with periods greater than ~24 h) are the main drivers of EWL in the idealized Thames Estuary during this storm. The semi-diurnal tides and surges in the estuary are strongly amplified and delayed by intertidal habitats, and these phase delays increase with increasing tide/surge frequency. Intertidal effects on lower-frequency tides and surges are minor. Intertidal habitats increase EWL by more than 0.1 m during the storm Xaver, which is mostly controlled by habitat-induced changes in the semi-diurnal tidal amplitudes and surge phases. Although the Thames Barrier closure effectively reduces flood risks upstream during this storm, it increases EWL by ~0.2 m in the outer estuary. Also, channel shallowing can reverse intertidal effects from raising to lowering EWL. Our findings reveal that intertidal habitats play a variable role across different tide and surge constituents, providing a critical scientific basis for understanding uncertainties associated with their effectiveness in estuarine flood risk mitigation.

1. Introduction

Flood hazards are increasingly threatening estuarine regions (Song et al., 2020) due to rising sea levels, extreme storms and river flows, and shifted tidal dynamics posed by climate change and human activities (e.g., reclamation, dredging, damming) (Arns et al., 2015; Zhang et al., 2021, 2023). Intertidal habitats, e.g., saltmarshes and mudflats, are invaluable ecological systems in estuaries, considering their co-benefits in mitigating flood/erosion, enhancing biodiversity, sequestering carbon, and filtering pollutants (Marsooli et al., 2016). However, because of sea-level rise and land reclamation, these habitats have been shrunk by more than 50 % worldwide since last century (Guo et al., 2022; Murray et al., 2019). Protecting, restoring, and creating intertidal habitats are increasingly proposed as sustainable, nature-based solutions to mitigate estuarine flood risks (Moraes et al., 2022), as implemented in the Ems and Scheldt estuaries (Li et al., 2016; Stark et al., 2017). Given the critical role of storm surges and tides in shaping estuarine hazards, it is essential to understand the role of intertidal habitats in storm-induced flooding for effective estuarine management.

Numerical studies have revealed the role of intertidal habitats in estuarine flooding during storm events can vary significantly across different estuaries. For instance, Gou et al. (2023) reported distinct effects of intertidal reclamation on flood risks in different areas of the Zhejiang coasts (China), which increase the maximum storm surges by about 0.3 m in Hangzhou Bay but reduce peak surges in smaller basins like Sanmen Bay. Other studies have suggested that intertidal habitats can have varying effects on storm-induced flooding under different storm conditions, introducing additional uncertainties into their flood

* Corresponding author.
E-mail address: xwei@noc.ac.uk (X. Wei).

https://doi.org/10.1016/j.ocemod.2026.102702
Received 10 October 2025; Received in revised form 22 January 2026; Accepted 6 February 2026
Available online 7 February 2026

mitigation potentials. Wamsley et al. (2010) found that the potential of wetlands to dampen surges in Mississippi River Delta (USA) is largely determined by the storm intensity and duration. Zhang et al. (2023) found that large-scale land reclamation combined with intensified storminess increases surge height in the Pearl River Estuary (China). However, by considering a different storm event in the same estuary, Shen et al. (2018) found that reclamation of intertidal areas have caused a reduction of surge height. The role of intertidal habitats on flood mitigation is also strongly dependent on intertidal habitat characteristics (e.g., location, elevation, width). Townend & Pethick (2002) reported that managed realignment (by allowing low-lying coastal areas to flood) in the inner Humber Estuary (UK) can reduce the extreme high water levels by 0.5–0.8 m. However, when implemented in the outer estuary, it tends to increase extreme high water levels by up to 0.2 m. Loder et al. (2009) found that, in the northern Gulf of Mexico, the lowered marsh elevation results in a decrease in storm-surge levels, while the reduction in marsh continuity (e.g., segmentation) is likely to raise coastal surge levels. The importance of intertidal habitat location is also confirmed by Stark et al. (2016), who found marshes at different locations along the Western Scheldt Estuary (Netherlands) reduce the extreme high water levels during storm events differently, which can even increase the extreme high water levels after extending the marsh platform. Kiesel et al. (2022) reported that increasing the width of the restored wetland (by managed realignment) in Freiston Shore (UK) leads to a more pronounced attenuation of surge waves, and expanding its vegetation cover can enable the dampening of even higher storm surges.

The variable impact of intertidal habitats on storm-induced flooding, which strongly depends on the characteristics of estuary, habitats, and forcings (Hu et al., 2015), highlight large uncertainties in the flood mitigation potentials of estuarine intertidal habitats. To reduce these uncertainties, it is important to understand the mechanisms by which intertidal habitats influence estuarine storm-induced flooding, such as through modulating different tidal and surge constituents, and to identify the processes that may explain the varying flood mitigation roles of intertidal habitats in estuaries.

Although numerical models have been widely used to reproduce complex estuarine processes, the high computational cost and complexity of numerical results lead to challenges in disentangling individual physical processes, particularly under a broad range of parameter space (Schuttelaars et al., 2013). Idealized semi-analytical (or analytical) models provide a computationally economical and effective means to systematically examine the physical processes that drive estuarine flooding (Chen et al., 2016; Dykstra et al., 2024; Familkhalili et al., 2020; Proudman, 1955; Reef et al., 2018; Talke et al., 2021; Wei et al., 2019). For example, Chen et al. (2016) developed a three-dimensional, idealized semi-analytical surge model, aiming to explore surge wave propagation within a semi-enclosed rectangular basin. Nevertheless, these idealized tide-surge models did not consider the effect of intertidal habitats, which are of great significance in estuarine hydrodynamics including tide and surge propagation. This significantly limits our ability to understand how intertidal habitats influence estuarine flooding, and to assess their flood mitigation potential under varying conditions of anthropogenic intervention and accelerated climate change.

In this study, we have two main goals: 1) to develop a three-dimensional, idealized semi-analytical tide-surge model, incorporating the dynamic interactions between subtidal and intertidal water motions under storm conditions; and 2) to explore the effect of intertidal habitats on storm-induced flooding in estuaries, and their roles in the individual tide and surge components that contribute to the flooding. This is achieved by extending the three-dimensional semi-analytical model of Chen et al. (2016) to resolve the dynamically coupled tidal and surge motions between intertidal and subtidal regions. The extended model was applied to the Thames Estuary during storm Xaver to demonstrate the varying roles of intertidal habitats in modulating tidal and surge components across different frequencies.

The paper is structured as follows: the model formulations and experiment design are introduced in Section 2; the model performance and intertidal effects on storm-induced estuarine flooding are investigated in Section 3; Section 4 briefly discusses the implications and limitations of this study; and conclusions are drawn in Section 5.

2. Methods

2.1. Model development and validation

To systematically examine the impact of intertidal habitats on estuarine flooding induced by storms, this study extends the three-dimensional (3D) semi-analytical model developed by Chen et al. (2016) to allow for the interactions between subtidal and intertidal waters. By assuming water depth is an order of magnitude larger than water level oscillations, Chen et al. (2016) resolved the 3D wind-induced surge dynamics in a semi-enclosed basin with no intertidal area. In the extended model, we consider an idealized estuary with intertidal habitats on both sides, where the water motion is described by the one-dimensional (1D) shallow water equations averaged over the intertidal cross-section. The dynamic interactions between the water motions in the 1D intertidal and 3D subtidal domains are resolved through a water exchange, F_n, across the interface between both regions. This interface (denoted as $\partial_F\Omega$, see Fig. 1) is termed as the intertidal-subtidal interface hereafter.

In this study, the area between the interface $\partial_F\Omega$ and the time-varying shorelines is termed as the intertidal region, while the area enclosed by $\partial_F\Omega$ (i.e., the channel and shoals) is termed as the subtidal region (Fig. 1a). The water depth over intertidal habitats is assumed to linearly decrease along the cross-estuary (y) direction, following Jay (1991),

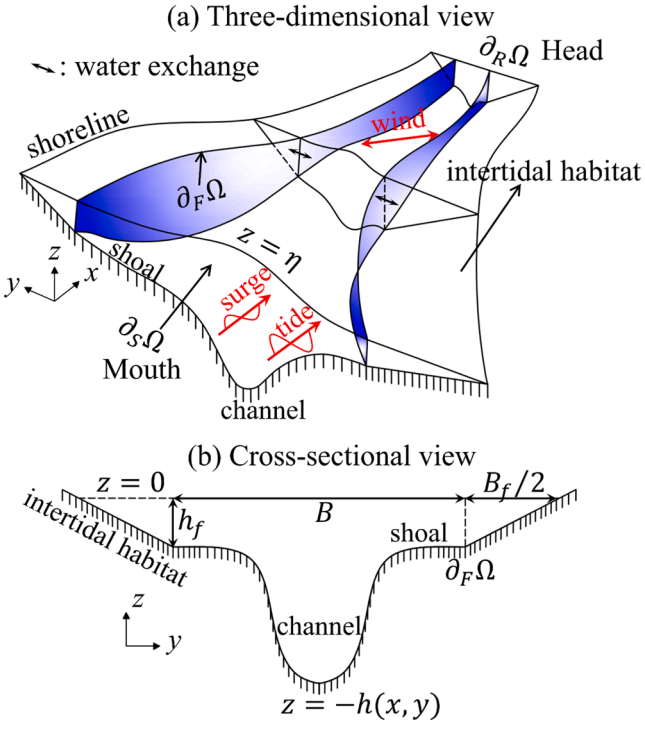

Fig. 1. (a) Three-dimensional view and (b) cross-sectional view of an idealized estuary considered in our model. The along-estuary, cross-estuary, and vertical dimensions are denoted by x, y, and z, respectively. The estuary is forced by tides and surges at the mouth, and wind stresses at the surface (red arrows). The landward and seaward boundaries are demonstrated by $\partial_R\Omega$ and $\partial_S\Omega$, respectively. The intertidal-subtidal interface $\partial_F\Omega$ is located at $y = \pm B/2$, where $B = B(x)$ represents the width of the subtidal region. The free surface is at $z = \eta$ and the estuarine bottom is at $z = -h(x, y)$.

with $B_f = B_f(x)$ as the intertidal habitat width at $z = 0$ and $h_f = h_f(x)$ the water depth at $\partial_F\Omega$ (Fig. 1b). The free surface elevation over intertidal areas, denoted as $\eta_f = \eta_f(x,t)$, describes the water level laterally averaged within the intertidal region.

In our model, water motions generated from nonlinear processes such as tide-tide, surge-surge, and tide-surge interactions in the estuary are not considered for simplicity. River-induced water level variations are also neglected, meaning that the nonlinear effects of tide-river or surge-river interactions on the water motion are excluded from the model. As shown in the sections below, the tide and surge water motions are separately calculated based on their corresponding linearized shallow water equations.

2.1.1. Three-Dimensional subtidal water motion

In our extended model, tide and surge water motions in the subtidal region are governed by the linearized 3D shallow water equations, as considered by Chen et al. (2016):

$$\nabla\cdot\mathbf{U} = 0, \tag{1}$$

$$\frac{\partial u}{\partial t} = fv - g\frac{\partial \eta}{\partial x} + \frac{\partial}{\partial z}\left(A_v\frac{\partial u}{\partial z}\right), \tag{2}$$

$$\frac{\partial v}{\partial t} = -fu - g\frac{\partial \eta}{\partial y} + \frac{\partial}{\partial z}\left(A_v\frac{\partial v}{\partial z}\right). \tag{3}$$

Here, t indicates time; the velocity vector $\mathbf{U} = (u, v, w)$ comprises the components u, v, and w in the x, y, and z directions; f denotes the Coriolis parameter; and g is the gravity acceleration. The vertical eddy viscosity $A_v(x,y)$ is assumed to be time independent and vertically uniform (Winant, 2007). The contributions of advection, baroclinic pressure gradient, and horizontal mixing are assumed to be of higher orders in our model, hence are omitted here, following Chen et al. (2016). The subtidal water motion described by Eqs. (1)-(3) can be separated into contributions due to tides (denoted by the subscript T) and surges (denoted by the subscript S), i.e., $\mathbf{U} = \mathbf{U}_T + \mathbf{U}_S$.

At the estuary mouth ($\partial_S\Omega$), the free surface elevation (η) is prescribed with several periodic tide (η_T) and surge components (η_S):

$$\eta = \eta_T + \eta_S = \Sigma_j A_{T_j}\cos\left(\sigma_{T_j}t - \varphi_{T_j}\right) + \Sigma_k A_{S_k}\cos\left(\sigma_{S_k}t - \varphi_{S_k}\right). \tag{4}$$

Here, the subscript j or k represents the index of each tide or surge component constituting the total water level η; A_{T_j}, φ_{T_j}, and σ_{T_j} are the amplitude, phase, and frequency of the tidal constituent η_{T_j}; A_{S_k}, φ_{S_k}, and σ_{S_k} are the amplitude, phase, and frequency of the surge component η_{S_k} at $\partial_S\Omega$. Since this model does not consider river discharge, the normal flux across the landward boundary ($\partial_R\Omega$) is required to vanish:

$$\int_{-h}^{\eta} \boldsymbol{u}_\mathrm{h}\cdot\mathbf{n}_\mathrm{h}\,dz = 0. \tag{5}$$

Here, $\boldsymbol{u}_\mathrm{h} = (u, v)$ represents the horizontal velocity vector, and $\mathbf{n}_\mathrm{h}$ indicates the horizontal unit normal vector directed outward. Different from Chen et al. (2016), the extended model allows a non-zero normal water flux across the intertidal-subtidal interface ($\partial_F\Omega$) that is coupled dynamically with intertidal water motions:

$$\int_{-h}^{\eta} \boldsymbol{u}_\mathrm{h}\cdot\mathbf{n}_\mathrm{h}\,dz = F_n. \tag{6}$$

Here, a positive value of F_n indicates a water flux directed toward intertidal habitats, and vice versa. Also, the extended model allows a discontinuous intertidal region along estuaries to consider local expansions or losses of these habitats. In such cases, the intertidal-subtidal water exchange becomes zero (i.e., $F_n = 0$) along estuarine segments without intertidal areas (i.e., with vertical walls and $B_f = 0$), as in Chen et al. (2016).

The kinematic and wind-shear stress boundary conditions are applied at the sea surface ($z = \eta$):

$$w = \frac{\partial \eta}{\partial t} + \boldsymbol{u}_\mathrm{h}\cdot\nabla\eta, \text{ and } A_v\frac{\partial \boldsymbol{u}_\mathrm{h}}{\partial z} = \frac{\boldsymbol{\tau}}{\rho}, \tag{7}$$

with ρ the water density and $\boldsymbol{\tau} = (\tau_x,\tau_y)$ the horizontal wind stress vector. The longitudinal and lateral wind stress (i.e., τ_x and τ_y) are represented by various periodic constituents

$$\left(\tau_x,\ \tau_y\right) = \Sigma_k\left(|\widehat{\tau}_{x_k}|,\ |\widehat{\tau}_{y_k}|\right)\cos\left(\sigma_{S_k}t - \varphi_{S_k} - \Delta\varphi_{S_k}\right),\ 0 \le t \le T. \tag{8}$$

Here, variables are marked with a hat (ˆ) to signify their complex amplitude; $|\widehat{\tau}_{x_k}|$ and $|\widehat{\tau}_{y_k}|$ denote the amplitude of the longitudinal and lateral wind stress driving each surge component (η_{S_k}), with $\left(\widehat{\tau}_{x_k},\ \widehat{\tau}_{y_k}\right) = \left(|\widehat{\tau}_{x_k}|,\ |\widehat{\tau}_{y_k}|\right)e^{-i\Delta\varphi_{S_k}}$; $i = \sqrt{-1}$ is the unit imaginary number; and $\Delta\varphi_{S_k}$ is the phase lag of the corresponding wind stress relative to η_{S_k} at the seaward boundary. The parameter T is the maximum wind duration/period, which is assumed to equal the maximum surge duration/period (Wei et al., 2019). In addition, the flow velocity normal to the estuarine bottom boundary ($z = -h$) is required to be zero due to impermeability, and a partial slip condition is implemented (Schramkowski and de Swart, 2002; Wei et al., 2018) based on the linearization of the bottom friction (Lorentz, 1926):

$$w = -\boldsymbol{u}_\mathrm{h}\cdot\nabla h, \text{ and } A_v\frac{\partial \boldsymbol{u}_\mathrm{h}}{\partial z} = s\boldsymbol{u}_\mathrm{h}. \tag{9}$$

Here, $s(x, y)$ denotes the slip parameter in the subtidal region, ranging from zero in frictionless or free-slip conditions to a large value under strongly frictional or no-slip conditions.

2.1.2. One-dimensional intertidal water motion

Tide and surge water motions over the intertidal region are described by the intertidal cross-sectionally averaged, linearized 1D shallow water equations [see also in Zhu et al. (2025)]. Like the subtidal water motion in Eqs. (2) and (3), nonlinear terms of higher orders and Coriolis deflection are neglected in the 1D intertidal model (see Appendix A):

$$\frac{\partial}{\partial x}\left(u_f\frac{h_f B_f}{4}\right) - \alpha F_n + \frac{B_f}{2}\frac{\partial \eta_f}{\partial t} = 0, \text{ with } \alpha = \sqrt{1 + \frac{1}{4}\left(\frac{dB}{dx}\right)^2}, \tag{10}$$

$$\frac{\partial u_f}{\partial t} = -g\frac{\partial \eta_f}{\partial x} + \underbrace{\frac{2}{h_f}\left(-s_f u_f + \frac{\tau_x}{\rho}\right)}_{M_R}. \tag{11}$$

Here, $u_f(x,t)$ represents the current velocity averaged within the intertidal cross-section, α is the estuary width convergence parameter, and $s_f(x)$ denotes the intertidal slip parameter. Eq. (10) demonstrates that the water exchange F_n across the interface $\partial_F\Omega$ is driven by two processes: i) the temporal variation of intertidal water storage (determined by η_f) and ii) the divergence of intertidal longitudinal flux (determined by u_f). The shear stress term averaged within the intertidal cross-section, M_R, consists of intertidal momentum loss/gain contributions due to bottom friction and surface wind shear. The intertidal water motion, as described by Eqs. (10) and (11), can also be separated into tide and surge contributions, i.e., $u_f = u_{f_T} + u_{f_S}$. At the mouth of the intertidal region, intertidal water level is assumed to equal the water level at the intertidal-subtidal interface [Eq. (4)]. At the head of the intertidal area, the water transport across this boundary is assumed to vanish, i.e., $u_f = 0$.

Two matching conditions are derived at the interface $\partial_F\Omega$ to ensure the continuity of the water mass and water level between subtidal and intertidal areas. The former condition is obtained by dynamically resolving the water exchange F_n between subtidal and intertidal areas.

Regarding the latter matching condition, following Zhu et al. (2025), the intertidal water level is assumed to change in the cross-estuary (y) direction linearly, and the lateral sea surface gradient is assumed to equal that at $\partial_F\Omega$. In comparison to a rigid lid approximation, our linear assumption accounts for the lagged water volume on the intertidal habitats induced by the lateral gradient of water level (Nidzieko and Ralston, 2012). Then, the laterally averaged intertidal water level (η_f) can be expressed by the subtidal water level (η) at the intertidal-subtidal interface ($\partial_F\Omega$),

$$\eta_f = \eta + \frac{\mathrm{sign}(y)\eta_y}{4}B_f, \text{ at } y = \pm\frac{B(x)}{2}, \tag{12}$$

with higher-order terms neglected (see Appendix A).

2.1.3. Semi-analytical approach

Following Chen et al. (2016) and Kumar et al. (2016), Eqs. (1)-(12) can be solved using a semi-analytical procedure. As a first step, estuarine water motions are divided into the tide-induced motion (ψ_T) and surge-induced motion (ψ_S), and the solutions of the system of equations are expressed in the form of

$$\psi = \psi_T + \psi_S = \Re\left\{\Sigma_j \widehat{\psi}_{T_j} e^{i\left(\sigma_{T_j} t - \varphi_{T_j}\right)} + \Sigma_k \widehat{\psi}_{S_k} e^{i\left(\sigma_{S_k} t - \varphi_{S_k}\right)}\right\}. \tag{13}$$

Here, ψ represents any unknown physical variable (η, u, v, w, η_f, and u_f), and $\Re\{\cdot\}$ indicates the real part of a complex variable. In our model, tides (ψ_T) are generated by external tidal forcing at the seaward boundary, neglecting the internally generated tidal constituents (e.g., overtides). Storm surge (ψ_S) results from i) an externally forced contribution driven by the surge forcing at the mouth and ii) an internally forced surge induced by the surface wind stress. As detailed in Appendix B, each tide or surge component can be solved separately by solving the individual linearized system of equations. Then, the extreme high water levels (referred to as EWL hereafter), defined as the maximum water level during the storm event, are calculated by summing the water level time series of the various tide and surge components during the event. This means that, intertidal habitats can modulate EWL by affecting each individual tide/surge contribution.

2.1.4. Model validation

The semi-analytically modeled water level in a simple test case is compared to that obtained from the numerical Delft3D model (Deltares, 2025) to illustrate the capabilities of the extended model. In the experiment designed for model comparison, the estuary length L is 60 km, and the subtidal region width B exponentially decreases landward,

$$B(x) = B_0 e^{-\frac{x}{L_b}}. \tag{14}$$

Here, $B_0 = 34$ km denotes the width of the subtidal region at the estuary mouth, and $L_b = 30$ km represents the width convergence length. Also, the subtidal region is represented by a flat channel bed with the water depth $h = 15$ m assumed spatially uniform for simplicity. Intertidal habitats are distributed on both sides of the entire estuary, with the depth at the intertidal-subtidal interface h_f set to 3 m. The width convergence of intertidal regions is determined by the ratio of the width of intertidal areas to the subtidal region width, i.e., $r_B = B_f/B$, which is prescribed as a constant (0.3) along the estuary. This means that, in this model experiment, the width convergence rate of the intertidal region (if present) equals that of the subtidal region. The vertical eddy viscosity ($A_v = 0.013$ m/s) and the slip parameters ($s = 0.04$ m/s, $s_f = 0.016$ m/s) are assumed to be temporally and spatially uniform (Wei et al., 2016). The Coriolis parameter f is prescribed as 10^{-4} rad/s, i.e., considering a latitude of 45°N. For simplicity, a semi-diurnal (M_2) tidal constituent with an amplitude of 2 m and a surge constituent with an amplitude of 1 m and a frequency of 3.5×10^{-5} s^{-1} (a quarter of the semi-diurnal frequency) are prescribed at the mouth. The river discharge at the head is ignored. At the surface, we prescribe a spatially uniform longitudinal wind stress with an amplitude of 1 Pa and a wind/surge period of 45 h, while the lateral wind stress is neglected.

A consistent setup of forcing conditions (e.g., tide, surge, wind) and estuary parameters (e.g., width, depth) is used in both the numerical and semi-analytical models. The primary difference is the treatment of bottom stress, which is linearized in the semi-analytical model but quadratic in the numerical one. To ensure comparability, the models are harmonized by equating their temporally averaged energy dissipation integrated within subtidal and intertidal areas. This requirement leads to the Lorentz linearization condition, which is used to derive the numerical model's quadratic friction coefficients from the semi-analytical results, see Zhu et al. (2025) for more details. The water level obtained from the semi-analytical model is a linear superposition of the tide and surge elevations, with different components solved separately. In the numerical model, however, water levels induced by tides and surges are calculated together with other physical processes unresolved in the semi-analytical model (e.g., advection, tide-surge interaction). The model parameters of the experiment designed for the model comparison are summarized in Table 1.

2.2. Experiment design

To assess the ability of the idealized semi-analytical model to reproduce storm-induced flooding in realistic estuaries, and to evaluate the potential role of intertidal habitats in influencing flood risks, we applied our extended semi-analytical model to the Thames Estuary, which is highly susceptible to storm-induced flooding.

2.2.1. Thames estuary

In this application experiment, parameters characteristic of the Thames Estuary, which is situated in the southeast of the UK, are considered. The Thames Estuary experiences an increasing flood risk due to rising sea levels and intensified storm events, where the primary threat of flooding is from the North Sea surge (Lavery and Donovan, 2005). Due to land reclamation, the intertidal ecosystem in the Thames Estuary has declined significantly, featuring a ~20 % reduction in salt marshes over the period 1973–1988 (Doody, 2004), leading to increased biodiversity risks and flooding threats (Richardson and Soloviev, 2021). To sustainably manage tidal flood risks and create climate resilient communities, intertidal habitats have been or are planned to be restored in the Thames Estuary, combined with other strategies like managed realignment, as part of the Thames Estuary 2100 Plan (Restemeyer et al., 2018, 2019).

The Thames Estuary includes an inner region with a length of ~120 km from Teddington to Foulness Island (Tye et al., 2018) and a ~30 km outer Thames region covering the southwest corner of the North Sea (Burningham and French, 2011), i.e., a total length of ~150 km with Teddington Weir at the tidal limit (O'Reilly-Wiese et al., 1997), see Fig. 2a. Its width decreases significantly from ~55 km at the estuary mouth to ~100 m at the head (see Fig. 2b). The Thames Estuary is representative of strongly convergent, tidally dominated, and

Table 1
Parameters of the experiment designed for model comparison.

Description	Parameters	Value	Unit
Estuary length	L	60	km
Subtidal estuary width at the mouth	B_0	34	km
Estuary convergence length	L_b	30	km
Channel depth	h	15	m
Depth at the intertidal-subtidal interface	h_f	3	m
Vertical eddy viscosity	A_v	0.013	m^2/s
Slip parameter in the subtidal region	s	0.04	m/s
Slip parameter over intertidal habitats	s_f	0.016	m/s
Coriolis parameter	f	10^{-4}	s^{-1}
Ratio of intertidal width to subtidal width	r_B	0.3	

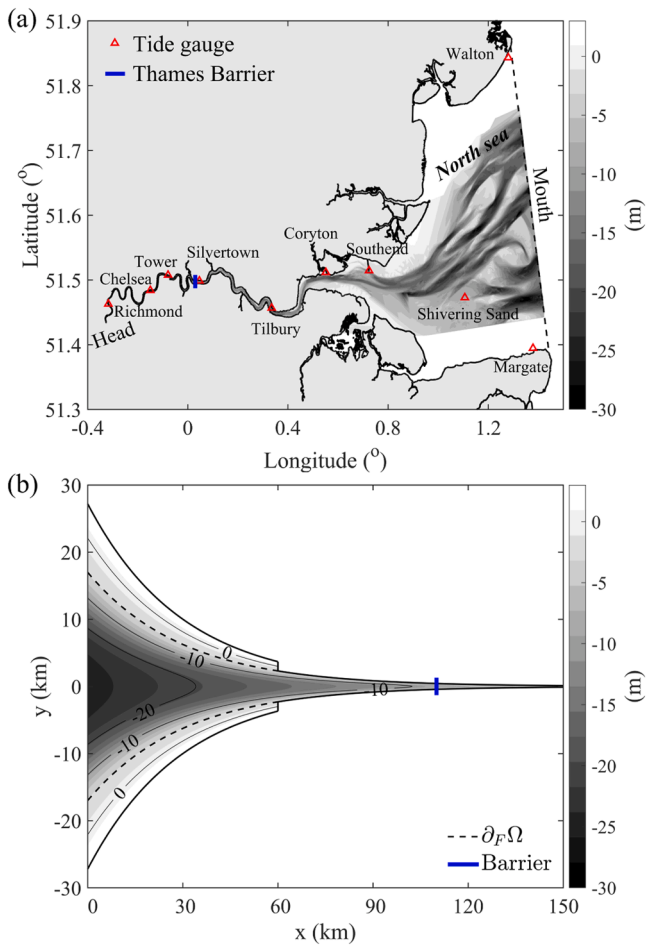

Fig. 2. The bathymetry and geometry of (a) the realistic and (b) idealized Thames Estuary. The red triangles show the tide gauges along the estuary, and the blue lines represent the Thames Barrier. The dashed lines in (b) represent the interface between subtidal and intertidal areas, $\partial_F\Omega$.

well-mixed estuaries (Friedrichs and Aubrey, 1994). It is macro-tidal with a tidal range of 5.3–3.3 m at Southend (Rossington and Spearman, 2009). The annual mean river runoff is low (~70 m^3/s), leading to a well-mixed water column over the entire tidal cycle (Mikhailov and Mikhailova, 2012).

The bathymetry and geometry in the idealized Thames Estuary are simplified from the observed data obtained from Port of London Authority (see Fig. 2b). The subtidal region width B is exponentially convergent landward as in Eq. (14). The subtidal region has a channel-shoal structure, where the water depth h decreases shoreward and landward,

$$h(x,y) = 0.5h_1(x)\left\{\tanh\left[k_s^2 - \left(k_s k_c \frac{y}{B}\right)^2\right] + 1\right\} + h_2(x) \text{ for } |y| \le B\Big/2. \tag{15}$$

Here, k_s and k_c characterize the bed slope and the width ratio between the shoal and the deep channel, respectively; and $h_1(x)$ and $h_2(x)$ are two depth functions defined by

$$h(x,\pm B/2) = 0.5h_1(x)\left[\tanh\left(k_s^2 - 0.25k_s^2k_c^2\right) + 1\right] + h_2(x) = h_f, \tag{16a}$$

$$h(x,0) = 0.5h_1(x)\left[\tanh\left(k_s^2\right) + 1\right] + h_2(x) = h_c^{\max}\left(1 - \frac{x}{L}\right) + h_c^{\min}\frac{x}{L}. \tag{16b}$$

Here, $h_c^{\max}$ and $h_c^{\min}$ denote the maximum and minimum water depth of the deep channel at the estuary mouth and head, respectively.

Intertidal habitats in the Thames Estuary are predominantly mudflats, composed mostly of fine silty sediment, with only limited sandy and vegetated areas (Musgrove et al., 2003; ABP Marine Environmental Research Ltd., 2013). These habitats are mainly located in the lower reaches (Fig. 2a), seaward of Canvey Island and Coryton (Grigg et al., 2025; Rossington and Spearman, 2009). For simplicity, the length of intertidal habitats is set to be 60 km with intertidal regions extending over the range of $0 \le x \le 60$ km (see Fig. 2b). The width ratio between the intertidal and subtidal regions (r_B) is prescribed as 0.3 in the idealized Thames Estuary (Friedrichs and Aubrey, 1994), while r_B is set to zero in the upper reaches without intertidal habitats ($x > 60$ km).

The subtidal slip parameter s is a hyperbolic tangent function of x determined by the bottom roughness variability along the estuary (Jalón Rojas et al., 2021), which is characterized by finer bed sediment distributing near the lower estuary and coarser bed sediment near the upper estuary,

$$s = 0.5(s_g - s_m)\left(1 + \tanh\frac{x - x_c^s}{x_l^s}\right) + s_m. \tag{17}$$

Here, s_g and s_m are the prescribed slip parameters in the upper and lower estuary, respectively, and x_c^s and x_l^s are length parameters determining the profile of the subtidal slip parameter. Given the finer sediment on intertidal mudflats relative to the channel, a smaller value is used for the intertidal slip parameter s_f (see Table 1) compared to the subtidal slip parameter (Soulsby, 1997).

2.2.2. Storm Xaver

Storm Xaver, which occurred on 5–7 December 2013 with a maximum wind duration/period (T) of ~45 h and is considered the most severe storm event in the North Sea over the past seven decades (Wei et al., 2019), is selected as the test case in our study. This event led to an EWL of more than 4 m in the North Sea, posing significant flood hazards along the east coast of the UK (Wadey et al., 2015). To prevent flood risk in London during the severe surges from the North Sea caused by the storm, the Thames Barrier near Silvertown (at $x = 110$ km, see Fig. 2) was closed (Spencer et al., 2015). This caused a significant drop in the EWL at locations upstream of the barrier during the storm (see Fig. C1, Appendix C), effectively reducing the flood risk in the upper tidal river (Kettle, 2020). The river discharge into the Thames Estuary during Xaver is less than 50 m^3/s, according to data from the National River Flow Archive (UK Centre for Ecology and Hydrology, 2025), with negligible effect on EWL as assumed in our model.

The total water levels were recorded by the tidal gauges (see red triangles in Fig. 2a) along the Thames Estuary, consisting of a predicted tidal elevation and a residual surge level calculated from subtracting the predicted tide from the total water level. Based on one month of the predicted tidal data, the tides are decomposed into several key components including O_1, K_1, N_2, M_2, S_2, and M_4 (Williams and O'Neill, 2024), by using T_TIDE for harmonic analysis (Pawlowicz et al., 2002), with the tidal residual omitted. Besides, the calculated residual surge levels during Xaver are also decomposed into various low-frequency signals (with frequencies of 0, ω, 2ω, 3ω, 4ω, 5ω, 6ω, and 7ω) by using a Fourier low-pass filter with a cut-off period of 6 h (Spicer et al., 2019), see Fig. 3. Here, $\omega = 2\pi/T$ represents the frequency of a surge component with a period equal to the wind duration T. Both the reconstructed tidal and surge levels show good agreement with the observations (see Fig. C2). The seaward boundary conditions for the tidal and surge forcings are obtained from tidal and surge decompositions of observed water levels at Margate (see Fig. 2a). In the Thames Estuary, the semi-diurnal M_2 tide is the most dominant component, with an amplitude of ~1.7 m at the mouth, while the surge component with a frequency of ω is the largest one during Xaver, with an amplitude of ~1 m (see Fig. 3b).

According to the ERA5 reanalysis wind data (Hersbach et al., 2020), the maximum wind speed in the Thames Estuary during storm Xaver was

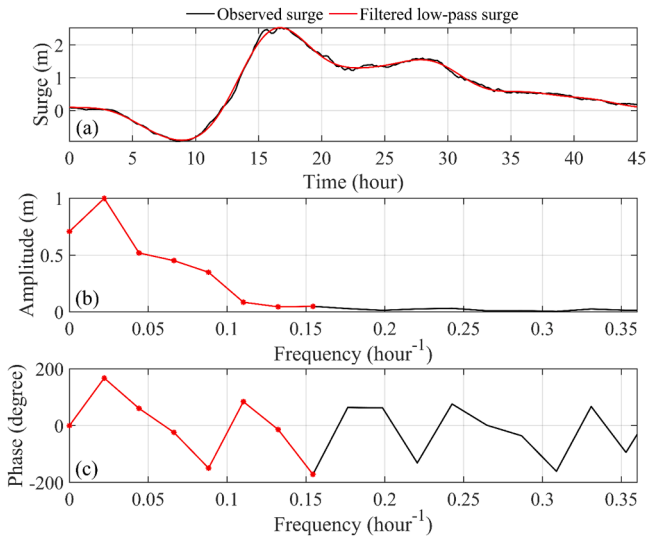

Fig. 3. (a) Time series of the surge, (b) surge amplitude, and (c) surge phase at Margate (estuary mouth) calculated by the Fourier low-pass filter with a cut-off period of 6 h. The black and red lines indicate the observed total surge level and the reconstructed low-frequency surge components from filtering the observed data. The red asterisks in (b) and (c) represent the prescribed amplitude and phase of surges at the mouth for different frequencies.

around 11–15 m/s, dominated by westerly winds, i.e., down-estuary (see Figs. C3 and C4). Therefore, in this study, the lateral wind stress is assumed to be zero (i.e., $\tau_y = 0$) to focus primarily on the along-estuary distribution of the water level driven by longitudinal wind stress. Besides, the wind stress is assumed to be spatially uniform and estimated from the domain-averaged wind speed within the Thames Estuary during Xaver (given its minimal spatial variability across the estuary, see Figs. C3 and C4), considering a constant surface drag coefficient for simplicity. Similar to the aforementioned Fourier low-pass filter for surge decomposition, the wind stress is also decomposed into several low-frequency components (Fig. 4). During Xaver, the maximum wind

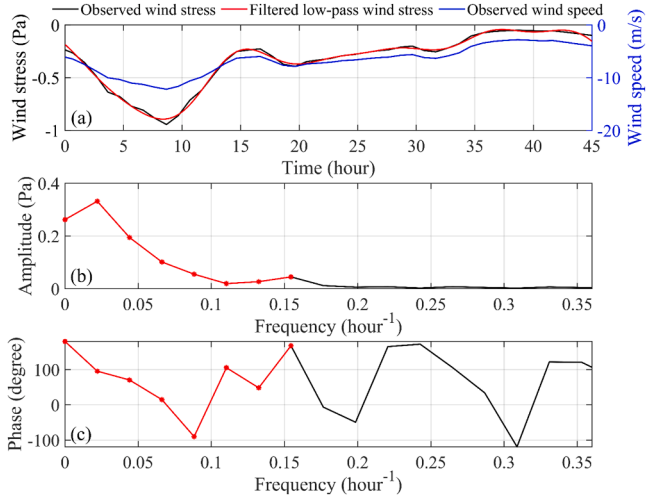

Fig. 4. (a) Time series of the domain-averaged wind stress, (b) wind stress amplitude, and (c) wind stress phase calculated by the Fourier low-pass filter with a cut-off period of 6 h. The black and red lines indicate the observed total wind stress and the reconstructed low-frequency wind stress components from filtering the observed data. The blue line represents the observed wind speed averaged over the Thames Estuary domain. The negative values of wind stress and wind speed in (a) imply seaward or down-estuary winds. The red asterisks in (b) and (c) represent the prescribed amplitude and phase of wind stress within the Thames Estuary for different frequencies.

stress (τ_{max}) in the Thames Estuary is approximately 1 Pa, corresponding to a wind speed of ~13 m/s (Fig. 4a), as considered in Wei et al. (2019) [see their Eq. (4)]. The surface wind forcings prescribed in the model, including the amplitude ($|\hat{\tau}_{x_k}|$) and phase ($\Delta\varphi_{S_k}$) of each wind component, are shown in Figs. 4b and 4c, respectively.

2.2.3. Model calibration

To represent the barrier closure during Xaver, the estuary length L is first set to 110 km in our model experiment, with the head located at the barrier, rather than using the full 150 km length up to the tidal limit. The idealized model of the Thames Estuary was calibrated by tuning the friction parameters A_v, s, and s_f. To assess the agreement between the modeled and observed water levels, three statistical indicators are calculated: the correlation coefficient (*CC*), the skill score (*SS*) (Willmott, 1981), and the root mean square error (*RMSE*), with

$$CC = \frac{\sum_{i=1}^{N}\left(\eta_i^m - \overline{\eta}^m\right)\left(\eta_i^o - \overline{\eta}^o\right)}{\sqrt{\sum_{i=1}^{N}\left(\eta_i^m - \overline{\eta}^m\right)^2 \sum_{i=1}^{N}\left(\eta_i^o - \overline{\eta}^o\right)^2}}, \tag{18}$$

$$SS = 1 - \frac{\sum_{i=1}^{N}\left(\eta_i^m - \eta_i^o\right)^2}{\sum_{i=1}^{N}\left(\left|\eta_i^m - \overline{\eta}^o\right| + \left|\eta_i^o - \overline{\eta}^o\right|\right)^2}, \tag{19}$$

$$RMSE = \sqrt{\frac{\sum_{i=1}^{N}\left(\eta_i^m - \eta_i^o\right)^2}{N}}. \tag{20}$$

Here, η_i^m and η_i^o denote the time series (i.e., during the storm event Xaver) of the modeled and observed water levels, respectively; the overbar ($\overline{\cdot}$) represents the mean value of the time series; and N is the length of the time series. Large values of *CC* and *SS* (close to 1), as well as small values of *RMSE* (close to 0), indicate a good agreement between the modeled and observed results.

Through a comparison of the modeled sea surface elevations to the data recorded at six tide gauges downstream of the Thames Barrier, $A_v = 0.013$ m^2/s, $s_g = 0.10$ m/s, $s_m = 0.04$ m/s, $x_c^s = 90$ km, $x_l^s = 15$ km, and $s_f = 0.016$ m/s were found to give the best fit. Note that the geometry and bathymetry in the outer 60 km region of the idealized Thames Estuary are identical to those in the experiment for model comparison (Table 1), except the subtidal water depth h with a channel-shoal structure where $k_c = 1.5$, $k_s = 1$, $h_c^{max} = 25$ m, and $h_c^{min} = 9$ m, see Eqs. (15) and (16).

2.2.4. Barrier closure

Given the strong dependence of estuarine hydrodynamics on estuary length (Wei et al., 2021), the reduction of estuary length caused by the closure of the barrier during Xaver can influence the propagation of tidal and surge waves, thereby modifying the EWL downstream of the barrier. To assess this effect, an experiment without the barrier is modeled in the Thames Estuary, i.e., considering a full estuary length of 150 km with tide and surge waves propagating up to the tidal limit (see Fig. 2).

2.2.5. Sensitivity to channel depth

To demonstrate the potential of our model, we conduct a sensitivity analysis to investigate the response of intertidal effects to channel depth changes, e.g., channel deepening (due to bed erosion or dredging) and channel shallowing (due to sediment deposition), which can significantly modulate estuarine water motion (Talke and Jay, 2020). In the sensitivity experiments, the maximum channel depth (h_c^{max}) is varied from 10 m to 30 m to investigate the sensitivity of the EWL to the channel depth.

In the experiment with or without barrier closure and in each sensitivity experiment with varying channel depth, two different scenarios, i.e., with ($r_B \neq 0$) and without (by setting $r_B = 0$ with vertical closed walls at $\partial_H\Omega$) intertidal habitats, are considered to examine the roles of intertidal areas in storm-induced flooding in estuaries. In both scenarios, all estuary parameters and boundary conditions are identical.

The key distinction between the two scenarios lies in the lateral water exchange, with $F_n = 0$ when intertidal habitats are excluded. Thus, the intertidal effects on storm-induced flooding in the idealized Thames estuary can be quantified by comparing the modeled water level in scenarios with and without intertidal areas.

3. Results

3.1. Model performance

The water level time series at different locations along the estuary obtained from the extended semi-analytical model are respectively compared against results from the numerical Delft3D model and the non-extended semi-analytical model developed by Chen et al. (2016) in which the intertidal regions are omitted (Fig. 5).

The water levels simulated with the extended model (black line) show strong agreement with those calculated from the numerical model (red asterisk, Fig. 5) along the estuary, with differences under 0.01 m. This demonstrates a minor nonlinear effect (e.g., advection) in the experiment considered here with a large water depth h. Meanwhile, the semi-analytical model requires much less computation time and memory usage compared to the numerical model, see detailed computational performance comparison in Table D1 (Appendix D). Therefore, compared to the numerical models, our extended semi-analytical model is more effective and computationally cheaper for systematic sensitivity studies where a broad range of parameter space can be investigated. In comparison with the semi-analytical model developed by Chen et al. (2016) (blue line, Fig. 5), the extended model that incorporates intertidal regions demonstrates a better capability to reproduce water levels under storm conditions, especially in the upper estuary. Neglecting the intertidal-subtidal interactions results in an underestimated (or overestimated) extreme high (or low) water level by up to 0.15 m near the estuary head (comparing black and blue lines, Fig. 5).

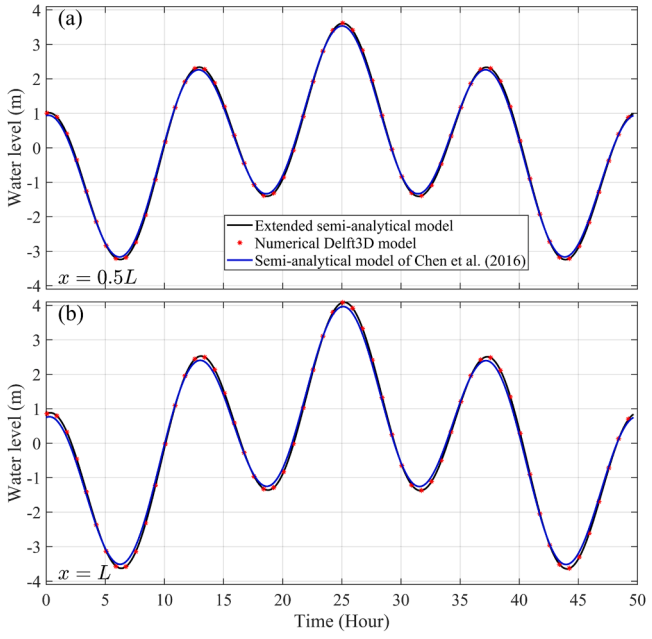

Fig. 5. Time series of water levels at (a) $x = 0.5L$ and (b) L, obtained from the non-extended semi-analytical model (blue line) developed by Chen et al. (2016) without intertidal areas, the numerical Delft3D model (red asterisk), and the extended semi-analytical model (black line) with intertidal areas.

3.2. Application to the Thames Estuary

3.2.1. Longitudinal distribution of tides, surges, and extreme high water levels

Our semi-analytical model well reproduces both the amplitude and phase of each of the main tide and surge components along the idealized Thames Estuary during storm Xaver (see Fig. 6). The amplitude of the predominant M_2 tide exhibits a substantial rise from ~1.7 m at the estuary mouth to ~2.7 m at the head (orange line, Fig. 6a). The other semi-diurnal (up to ~0.5 m) and quarter-diurnal/diurnal (~0.1 m) tidal components are much weaker. During Xaver, the predominant surge amplitude at a frequency of ω (i.e., with a period of ~45 hours) remains nearly constant along the estuary (~1 m, blue line in Fig. 6c). The other surge components with $\sigma_S \leq 4\omega$ are also significant, with an amplitude of ~0.4–0.8 m. The higher-frequency surges with $\sigma_S \geq 5\omega$, however, are relatively weaker (~0.2–0.4 m) along the estuary, with their amplitudes increasing landward. The phase of each tide or surge component increases landward, and its increasing rate becomes greater as the tide and surge frequencies increase (Figs. 6b and 6d).

The modeled total water level, calculated from the superposition of all tide and surge components, also aligns well with the observed data, though the low water levels are slightly underestimated by our semi-analytical model, particularly in the upper estuary (Figs. 7a–f). For the modeled and observed sea surface elevations, the correlation coefficient (*CC*), the skill score (*SS*), and the root mean square error (*RMSE*) averaged over all tide gauges (see red triangles in Fig. 2a) are 0.9906, 0.9870, and 0.2365 m, respectively (see Table 2), confirming the good performance of our semi-analytical model. The simulated EWL is around 4–4.5 m along the estuary, which is also consistent with observations (Fig. 7g).

3.2.2. Dominant drivers of extreme high water levels

To identify the main drivers of the EWL in the Thames Estuary during Xaver, the contribution of each tide and surge component to the total EWL was investigated. Fig. 8 shows the difference between the total EWL and that excluding one of the tide/surge components. The predominant M_2 tide contributes to a great increase in the EWL (~0.7–1.5 m, orange line in Fig. 8a). The other semi-diurnal components (i.e., N_2 and S_2) also result in an increase of ~0.5 m in the EWL (green and yellow lines, Fig. 8a). The contributions of quarter-diurnal/diurnal tides to the EWL are minor. The overall contribution of all tidal components leads to an increase in the EWL of around 0.7–1.6 m, which decreases landward (black line, Fig. 8a), following a similar pattern to that of the dominant M_2 tidal constituent (compare orange and black lines in Fig. 8a).

Depending on the phase offset between the dominant tide and surge constituents, the surge can either increase or decrease the EWL due to peak-peak superposition or peak-trough offset, respectively. For example, the low-frequency surge components with $\sigma_S \leq 2\omega$, considering both externally forced and internally wind-induced contributions, contribute to a significant increase in the EWL (~0.5–0.8 m), while the other higher-frequency components (e.g., $\sigma_S = 4\omega$) lead to a decrease of more than 0.6 m in the EWL (Fig. 8b). The total surge contribution results in an increase in the EWL of around 0.1–1.6 m, which significantly decreases toward the estuary head (see black line in Fig. 8b). This is because high-frequency surges increasingly contribute to lowering EWL while low-frequency surges contribute less to raising EWL in the upper reach (see Fig. 8b). The effects of different tide and surge constituents on the EWL indicate that the dominant semi-diurnal tides and lower-frequency surges are the main factors inducing the high EWL in the Thames Estuary during Xaver.

As discussed in Wei et al. (2019), the coastal flooding around the North Sea (outside of the Thames Estuary) during Xaver is predominantly controlled by the surge internally generated by the local surface wind forcing. Within the Thames Estuary, however, the externally forced contribution dominates over the internally wind-induced contribution during Xaver, except for the minor higher-frequency

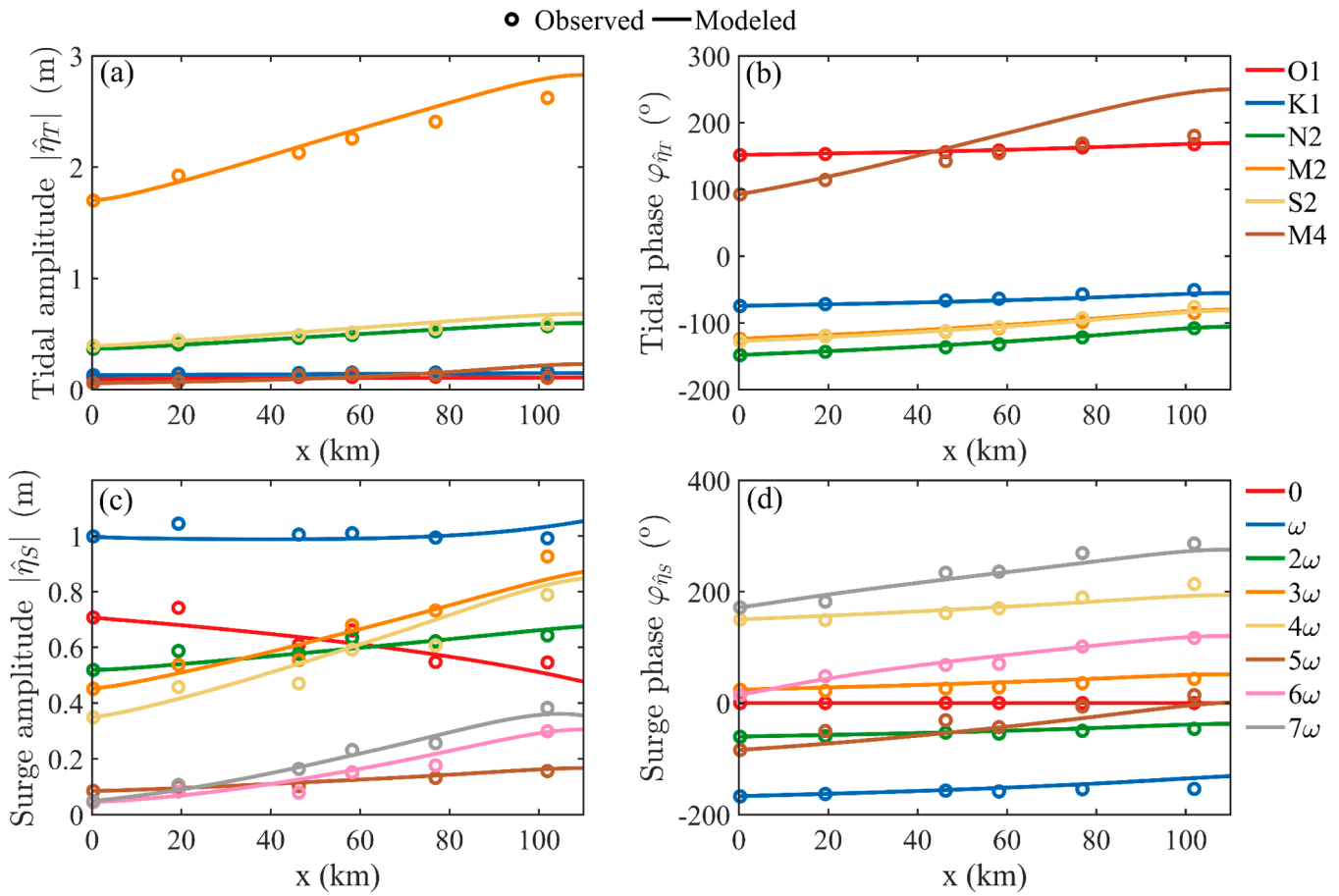

Fig. 6. The comparison of the amplitude (left column) and phase (right column) of each (a),(b) tide and (c),(d) surge component between the observed (circles) and modeled (lines) results.

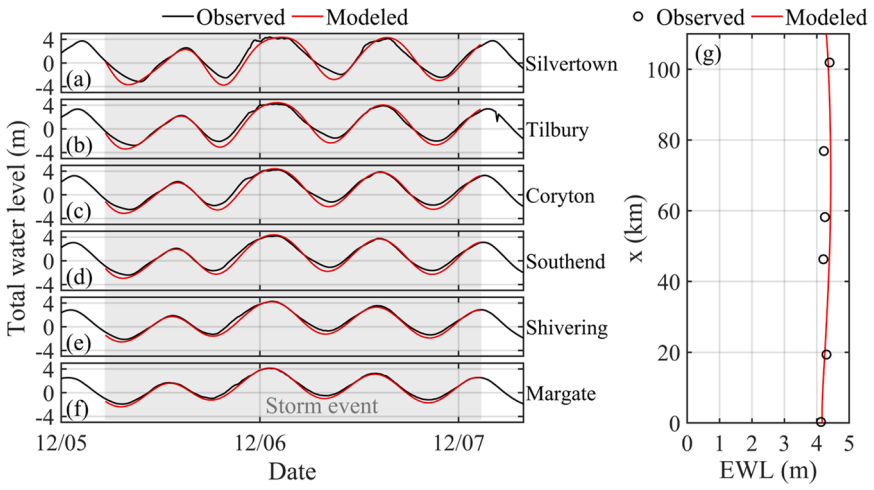

Fig. 7. (a–f) Time series of the total water level and (g) extreme high water level (EWL) during storm Xaver at the six tide gauges from Silvertown near the Thames Barrier to Margate at the mouth. The black line/circle and the red line represent the observed and modeled water levels, respectively. The gray box denotes the period during which the storm Xaver occurred.

surges with $\sigma_S \geq 6\omega$ where both contributions are comparable (see Fig. E1, Appendix E). This is reasonable, as the Thames Estuary is located far from the center of the storm, which was positioned at the northern end of the North Sea (see Fig. C3). Consequently, the external surge forcing generated in the North Sea and propagating into the mouth of the Thames Estuary surpasses the local wind forcing within the estuary. For completeness, our following analysis of the intertidal effects on EWL considers both externally forced and internally generated surge contributions.

3.2.3. *Intertidal effects on extreme high water levels*

The intertidal effects on the tide/surge and extreme high water levels are quantified by the difference in the total tide η_T, total surge η_S, and EWL between scenarios that include and exclude intertidal regions ($\Delta\eta_T$,

Table 2
Correlation coefficient (*CC*), the skill score (*SS*), and the root mean square error (*RMSE*) for the modeled total water level at each tide gauge.

Gauge station	*CC*	*SS*	*RMSE* (m)
Silvertown	0.9781	0.9792	0.3489
Tilbury	0.9896	0.9866	0.2617
Coryton	0.9897	0.9852	0.2582
Southend	0.9933	0.9888	0.2160
Shivering	0.9950	0.9901	0.1839
Margate	0.9980	0.9924	0.1501
Average	0.9906	0.9870	0.2365

$\Delta\eta_S$, and ΔEWL). Fig. 9 shows that intertidal habitats affect the EWL through modifying the temporal variations of tide and surge levels. The presence of intertidal areas results in an increase of ~0.3 m or a decrease of ~0.25 m in the total tidal elevation along the estuary (Fig. 9a). This habitat-induced change exhibits a semi-diurnal frequency variation with nearly four peaks and troughs during the 45-hour storm event. This indicates that the intertidal regions modulate the tide mainly through its dominant semi-diurnal components.

The presence of intertidal areas also leads to a change of the overall surge level by up to 0.25 m along the estuary (Fig. 9b). This change shows an even higher-frequency variation with more than six peaks and troughs during the event, suggesting that these habitats modulate the surge mainly through its higher-frequency components, rather than its predominant low-frequency component. The changes in surge levels due to intertidal habitats are most pronounced around hour 18–20 along the estuary (Fig. 9b), when the surge height reaches its peak during the storm (see Fig. 3a and Fig. C2, right column).

Due to intertidal effects, the peak tidal height during the storm is increased by up to 0.17 m at the head (red line, Fig. 9c), and the peak surge height is elevated by ~0.1 m around $x = 60$ km (blue line, Fig. 9c). Consequently, these intertidal habitats lead to an increase in the EWL of more than 0.1 m along the idealized Thames Estuary during the storm (black line, Fig. 9c).

3.2.4. *Intertidal effects on individual tide and surge contributions*

The intertidal area influences the time-varying tide and surge elevations through modifying the amplitude and phase of each tide and surge constituent (see Fig. 10). The predominant M_2 tidal amplitude is increased by as much as 0.12 m because of the presence of intertidal areas (orange line, Fig. 10a), with a phase delay of up to 3° (orange line, Fig. 10b). The other semi-diurnal tidal oscillations (i.e., N_2 and S_2) are also enhanced by these habitats, with their phases delayed slightly (green and yellow lines, Figs. 10a and 10b). The quarter-diurnal M_4 tide is also amplified slightly, and its phase is increased by up to 14° (brown line, Figs. 10a and 10b). However, the diurnal tides (red and blue lines, Figs. 10a and 10b) are hardly changed by intertidal habitats. It is worth noting that the tidal phase delay due to intertidal habitats shows similar values for tidal components with close frequencies [e.g., diurnal (O_1 and K_1) or semi-diurnal (N_2, M_2, and S_2) tides], and the delay increases with tidal frequency.

The surge component with $\sigma_S = 4\omega$ or 3ω experiences the largest amplitude increase of ~0.02–0.04 m when including intertidal habitats (yellow and orange lines, Fig. 10c). The amplitudes of the other surge constituents are increased by less than 0.02 m, with the mean surge nearly unchanged. Meanwhile, intertidal habitats cause a slight decrease of ~0.02 m in the amplitude of the surge component with $\sigma_S = 7\omega$ in the upper estuary (gray line, Fig. 10c). The delay in the surge phase caused by intertidal habitats shows a strong sensitivity to the surge frequency (Fig. 10d), with higher-frequency surges delayed more (by up to 14° for the surge component with $\sigma_S = 7\omega$, gray line in Fig. 10d).

Note that the surge components with $\sigma_S = 4\omega$ and 3ω have periods of 11.3 h and 15.1 h, respectively, close to that of the M_2 tide (12.4 h). This means that the tide and surge constituents near the semi-diurnal frequency are mostly affected by intertidal habitats in terms of amplitude. Also, the tide and surge propagations are delayed along the estuary by intertidal habitats, which is most pronounced for higher-frequency components. These results demonstrate that intertidal habitats affect the amplitude and phase differently across different tide and surge components.

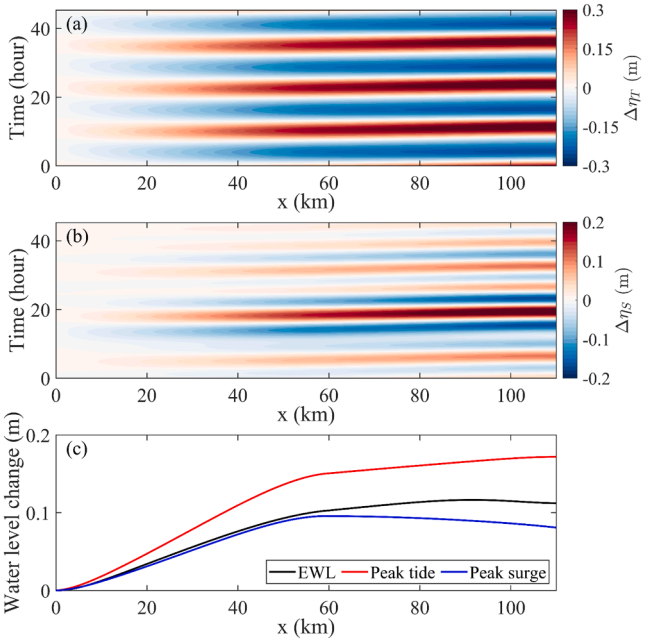

Fig. 9. Intertidal effect on (a) the time series of tidal level, (b) the time series of surge level, and (c) the extreme high water levels (EWL, black), peak tidal height (blue), and peak surge height (red).

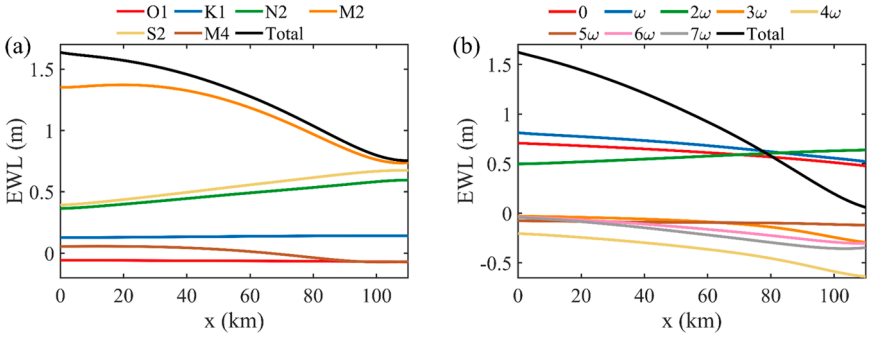

Fig. 8. The contribution of each (a) tide and (b) surge component to the extreme high water levels (EWL). The black lines indicate the combined effects of (a) all tidal components and (b) all surge components on the EWL.

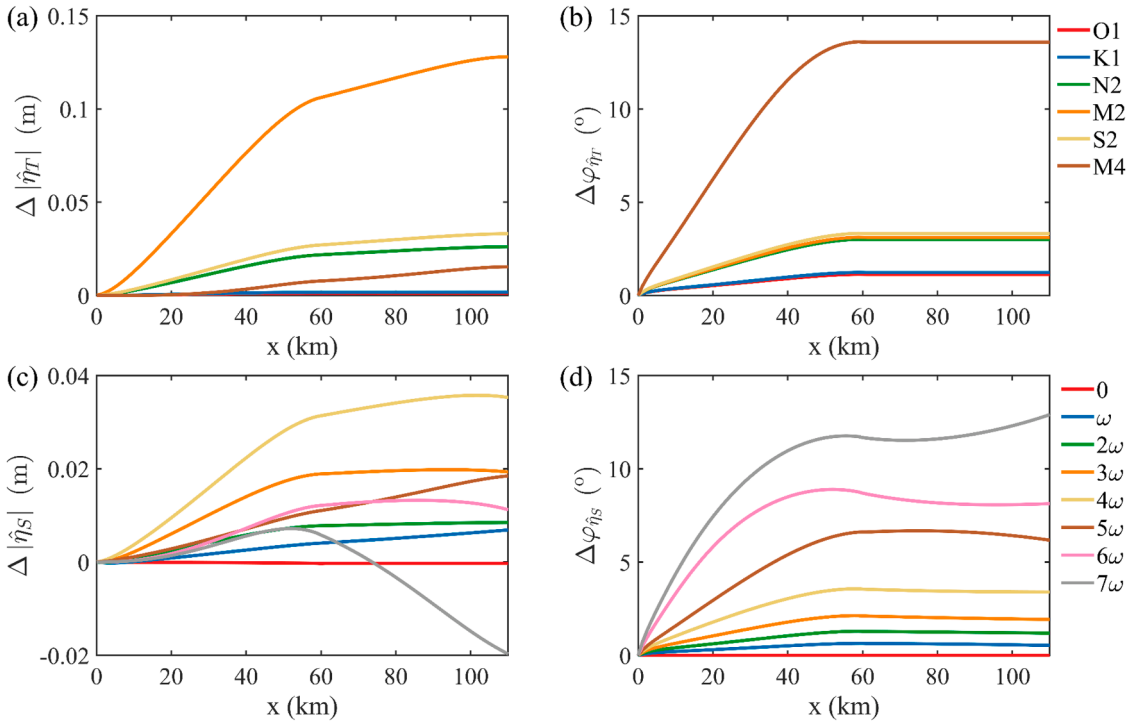

Fig. 10. Intertidal effect on the amplitude (left column) and phase (right column) of each (a),(b) tide and (c),(d) surge component.

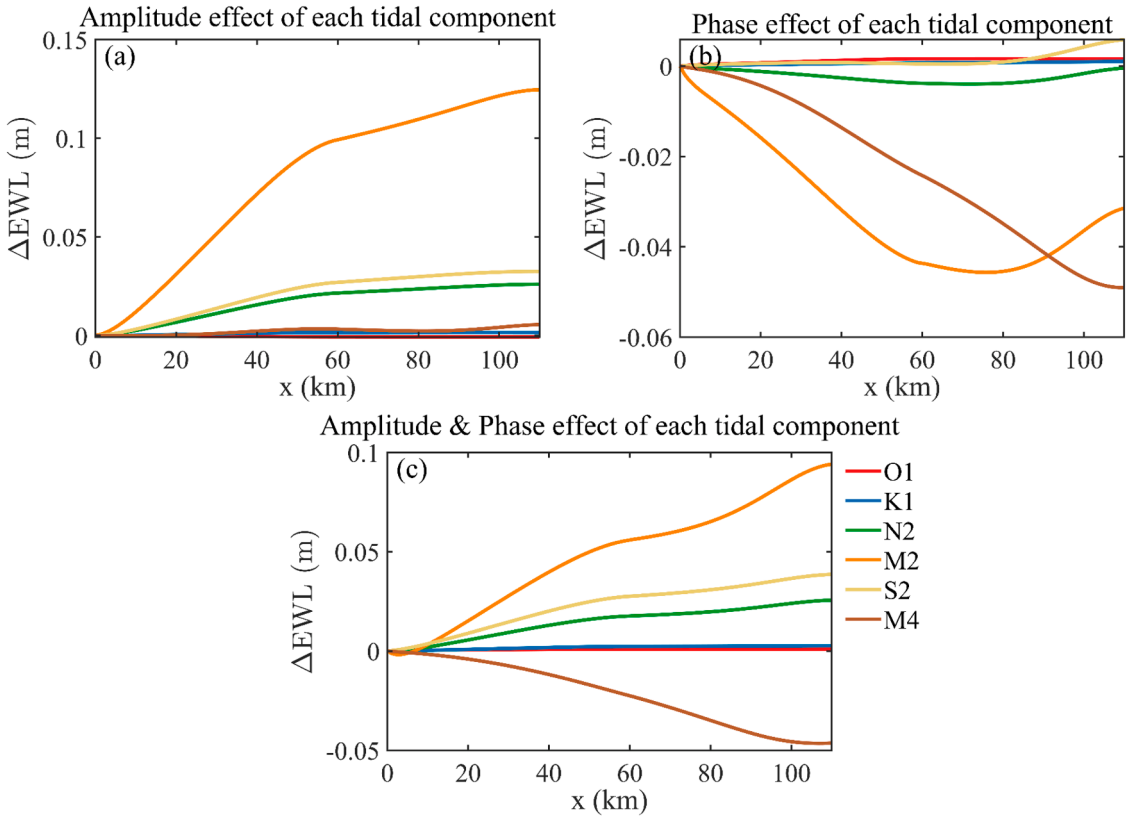

Fig. 11. Intertidal effects on the extreme high water levels (EWL) due to habitat-induced tidal changes in the (a) amplitude, (b) phase, and (c) both amplitude and phase of each tidal component.

3.2.5. Mechanisms of intertidal habitats affecting extreme high water levels

To understand the contribution of habitat-induced changes in tides and surges to the EWL, the EWL change (ΔEWL) induced by intertidal habitats associated with individual contributions of each tide/surge component is calculated. This is achieved by subtracting the EWL calculated from all tide and surge components without any intertidal habitat from that obtained by considering only the habitat-induced change in the amplitude and/or phase of a single tide/surge component (Figs. 11 and 12). Our results show that, the intertidal habitats cause an increase of more than 0.12 m in the EWL by modifying the M_2 tidal amplitude (orange line, Fig. 11a) but decrease the EWL by up to 0.04 m through changing the M_2 tidal phase (orange line, Fig. 11b). Overall, the habitat-induced changes in both M_2 tidal amplitude and phase leads to an increase of up to 0.09 m in the EWL along the estuary (orange line, Fig. 11c). Changes in the other semi-diurnal tidal components (i.e., N_2 and S_2) also cause an increase of ~0.03 m in the EWL, mainly through habitat-induced changes in their amplitudes (green and yellow lines, Fig. 11). The contribution of habitat-induced changes in diurnal components to the EWL is less than 0.01 m (red and blue lines, Fig. 11). Changes in the quarter-diurnal M_4 tidal component lead to a decrease of up to 0.04 m in the EWL (brown line, Fig. 11c), primarily through the habitat-induced change in its phase (brown line, Figs. 11a-b). Consequently, the habitat-induced changes in the amplitudes of all tidal components, dominated by the M_2 component, cause an increase of up to 0.19 m in the EWL (red line, Fig. 13a). In contrast, the overall tidal phase changes due to intertidal habitats, dominated by the M_4 and M_2 components, lead to a decrease of ~0.07 m in the EWL (blue line, Fig. 13a). The overall habitat-induced tidal changes contribute to an increase of up to 0.13 m in the EWL (black line, Fig. 13a).

The contribution of habitat-induced changes in surges to the EWL is relatively smaller than that of tides (see Fig. 12). Changes in the surges with $\sigma_S = 3\omega$ and 4ω cause an increase of up to 0.03 m in the EWL (orange and yellow lines, Fig. 12c), mainly through their phase changes induced by intertidal effects (orange and yellow lines, Figs. 12a-b). Changes in the higher-frequency surges with $\sigma_S = 6\omega$ and 7ω, however, lead to a decrease of less than 0.02 m in the EWL (pink and gray lines, Fig. 12c), through habitat-induced changes in their amplitudes and/or phases (pink and gray lines, Figs. 12a-b). The habitat-induced changes in the other surges have minimal impact on the EWL. Consequently, the habitat-induced changes in the amplitudes of all surge components, dominated by the surge of $\sigma_S = 4\omega$, lead to a decrease of less than 0.04 m in the EWL (red line, Fig. 13b). In contrast, the phase changes due to intertidal habitats, dominated by the surge of $\sigma_S = 3\omega$ or 4ω (near the semi-diurnal frequency), induce a significant increase in the EWL of up to 0.08 m (blue line, Fig. 13b). The overall habitat-induced surge change results in an increase of up to 0.07 m in the EWL along the estuary (black line, Fig. 13b).

These results confirm the varying roles of intertidal habitats in modulating the EWL through affecting different tide and surge constituents. The semi-diurnal tidal components contribute significantly to the EWL increase (see Fig. 8a), thereby the enhanced semi-diurnal tides due to intertidal habitats also considerably increase the EWL (Fig. 11a). Although the lower-frequency surges with $\sigma_S \leq 2\omega$ can contribute significantly to the increase in the EWL (Fig. 8b), the habitat-induced changes in these surge components are minor (Figs. 10c-d), thereby these changes only slightly affect the EWL (see Fig. 12c). The higher-frequency surges, however, tend to decrease the EWL during Xaver (Fig. 8b). Therefore, the intertidal habitat can decrease the EWL through amplifying the higher-frequency surge components (e.g., the surge of $\sigma_S = 4\omega$, see Fig. 12a) or increase the EWL through delaying these components (e.g., the surge of $\sigma_S = 3\omega$ or 4ω, see Fig. 12b).

3.2.6. Impact of the Thames Barrier closure

The closure of the Thames Barrier during Xaver significantly

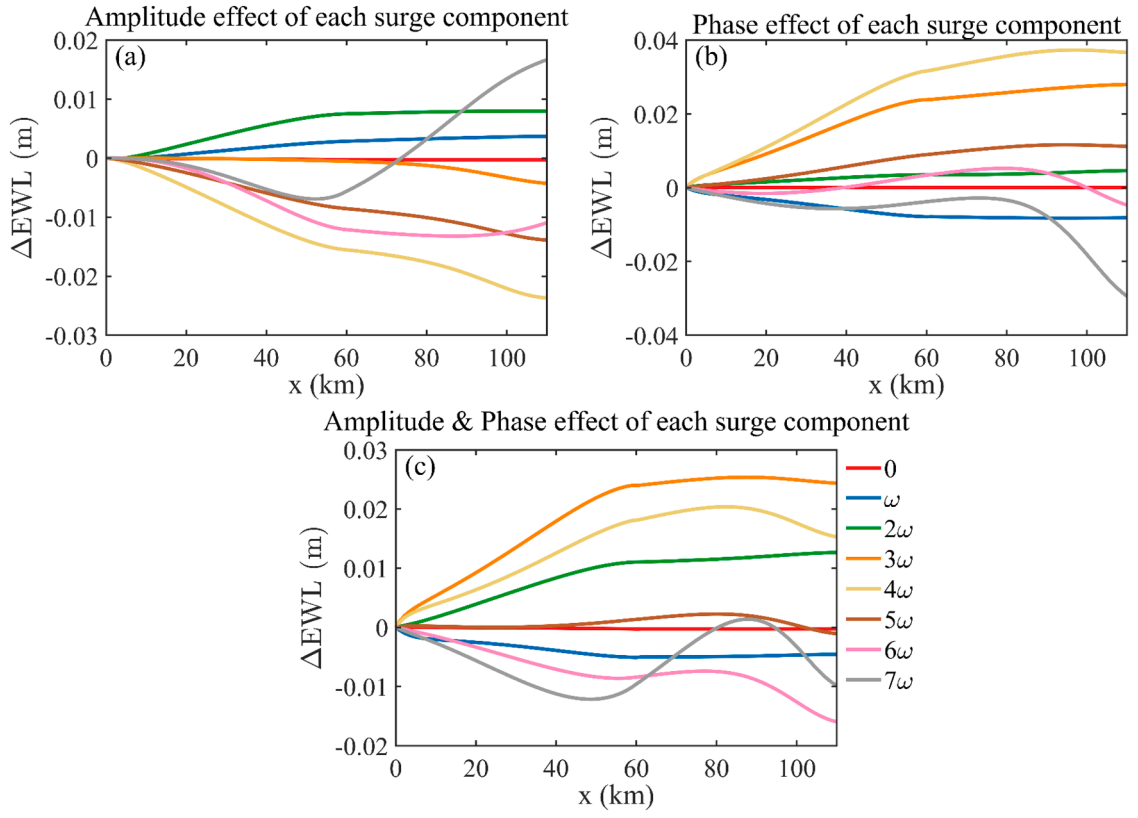

Fig. 12. Intertidal effect on the extreme high water levels (EWL) due to habitat-induced surge changes in the (a) amplitude, (b) phase, and (c) both amplitude and phase of each surge component.

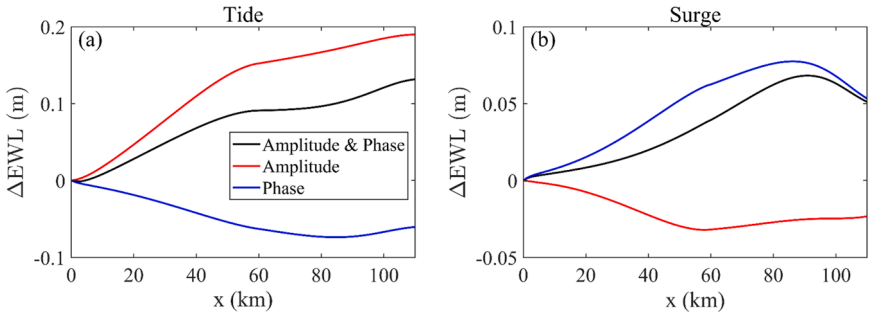

Fig. 13. Intertidal effect on the extreme high water levels (EWL) due to habitat-induced changes in amplitude (red), phase (blue), and both amplitude and phase (black) for all (a) tidal and (b) surge components.

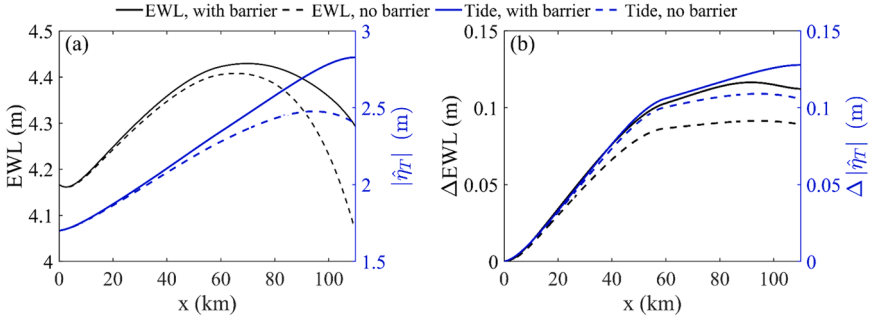

Fig. 14. (a) The along-estuary distribution of the extreme high water levels (EWL, black lines) and the amplitude of the predominant M_2 tide (blue lines), and (b) the intertidal effects on both variables, in experiments that close (solid lines) and open (dashed lines) the storm surge barrier.

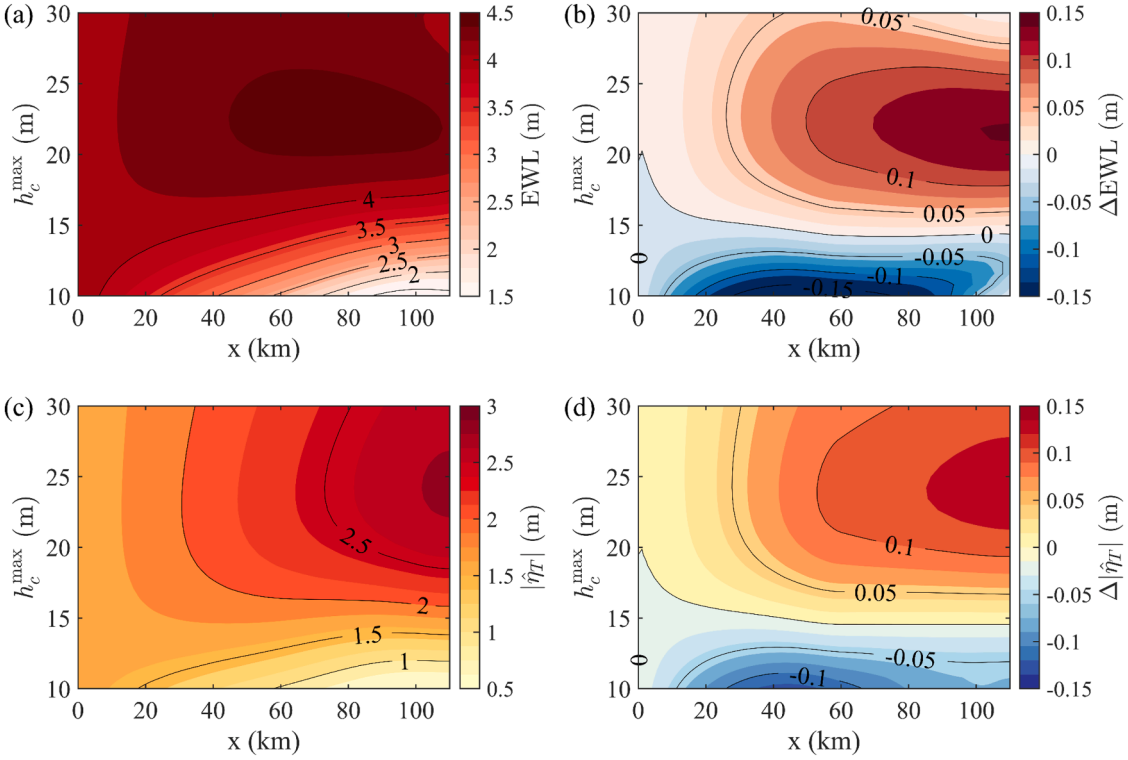

Fig. 15. Response of (a) extreme high water levels (EWL), (c) the amplitude of the predominant M_2 tide, and (b), (d) the intertidal effects on both variables to changes in the maximum channel depth (h_c^{max}).

modulates the storm-induced flooding in the Thames Estuary by reducing the estuary length. Without the barrier closure, the EWL is considerably decreased by up to 0.2 m at $x = 110$ km, and the habitat-induced increase in the EWL is also slightly decreased by ~0.03 m (compare black solid and dashed lines in Figs. 14a and 14b). This can be explained by the dampening of tide (e.g., the predominant M_2 tide, see blue lines in Fig. 14a) and surge (not shown here) waves within a longer estuary (Wei et al., 2021). For instance, in the absence of the barrier, the M_2 tidal amplitude is significantly decreased by up to 0.4 m, with intertidal effects on it also slightly decreased (compare blue solid and dashed lines in Figs. 14a and 14b). Therefore, the tidal and surge wave oscillations are weakened considerably when considering the barrier not closed, resulting in a reduced EWL and weakened intertidal effects on the EWL.

During the storm Xaver, the effects of intertidal areas on the EWL in the Thames Estuary are comparable to those induced by barrier closure, both causing an increase in the EWL of ~0.1 m downstream of the Thames Barrier (Fig. 14). Although the barrier closure during the storm effectively reduces the EWL in the upper tidal river (see Fig. C1), it increases the EWL and the associated flood risks in regions downstream of the barrier.

3.2.7. Impact of the channel depth change

The tide and surge wave propagations along the idealized Thames Estuary, as well as the EWL, are strongly affected by the channel depth changes. By increasing the maximum channel depth (h_c^{max}) from 10 m to 30 m, the tide waves (e.g., the predominant M_2 tide, see Fig. 15c) and surge waves (not shown here) are amplified, thereby the resulting EWL is significantly increased from ~1.5 m to 4.5 m (Fig. 15a). This implies that shallowing the channel can effectively reduce flooding in the idealized Thames Estuary, as has also been found for the Jamaica Bay (USA) by Orton et al. (2015).

More importantly, the roles of intertidal habitats in modulating the EWL reverse when increasing the channel water depth. In shallow systems (e.g., $h_c^{max} = 10$–15 m), intertidal habitats tend to decrease the EWL by more than 0.15 m (Fig. 15b). In deep systems (e.g., $h_c^{max} = 15$–30 m), however, intertidal habitats result in an increase in the EWL of up to 0.15 m along the estuary. This is due to the differing effects of intertidal areas on tide and surge wave propagation in shallow versus deep estuaries. Our results demonstrate that intertidal habitats tend to dampen tide (e.g., the predominant M_2 tide, see Fig. 15d) and surge waves (not shown) in shallow systems, but amplify them in deep systems.

The reversal of intertidal effects on tides and surges between shallow and deep estuaries can be explained by differences in the resonance characteristics of long-wave propagation in estuaries of different water depths. Since the sensitivity of surge amplitude to water depth (not shown) is similar to that of tides, the discussion here focuses on tidal long waves. By including intertidal areas on both sides of the estuary, the mean water depth over the total cross-section is effectively reduced, leading to a decrease in tidal wavelength (Zhu et al., 2025). In shallow systems, the tidal wavelength is small due to a small water depth, and the estuary length exceeds the quarter-wave resonance length. Hence, the reduction in tidal wavelength due to the inclusion of intertidal areas pushes the system further from the quarter-wavelength resonance, causing the damping of tidal waves. In deep systems, however, the estuary length is shorter than the quarter-wave resonance length due to a large water depth. The reduced tidal wavelength, resulting from the inclusion of intertidal areas, brings the estuary length closer to the quarter-wave resonance length, hence causing the amplification of tides. The contrasting roles of intertidal areas identified here are analogous to the long-wave amplitude response to reduced water depth reported by Talke and Jay (2020).

4. Discussion

4.1. Implications

Our results suggest that the existence of intertidal areas significantly increases peak tide and surge elevations, thereby elevating the EWL in the idealized Thames Estuary during storm Xaver (see Fig. 9c). This appears to contradict the broad consensus about the flood-mitigation function of estuarine intertidal habitats due to their role in dissipating wave energy (Barbier et al., 2011; Möller et al., 2014; Orton et al., 2015; Reed et al., 2018). This discrepancy can be understood as these previous studies mostly focused on the localized wave attenuation effect of intertidal regions, i.e., storm surges are dampened within these habitats when propagating shoreward across intertidal areas (Grant and Cooker, 2023; Smolders et al., 2015). In contrast, our study examines the effects of intertidal areas on tidal and surge propagation along the whole estuary, which can either amplify or attenuate storm-induced flooding while propagating landward, such as those discussed in Section 1.

The varying role of intertidal habitats on storm-induced flooding, as derived in this study, suggests that the effectiveness of creating and restoring intertidal habitats for flood mitigation cannot be guaranteed across all systems. Moreover, the impact of intertidal habitats on the EWL, through altering each long-wave component, can vary across estuaries with different tide, surge, and wind forcings. For example, intertidal habitats can increase the EWL by increasing the tidal amplitude and surge phase but decrease the EWL by increasing the surge amplitude and tidal phase (see Fig. 13). Besides, our results in Section 3.2.7 demonstrate that the intertidal effects on flooding can shift from reducing to increasing the EWL as channel depth increases. This may explain the contrast roles of intertidal habitats in storm-induced estuarine flooding, depending on the different forcing conditions and estuary characteristics. Our results in Sections 3.2.3 and 3.2.6 also imply that intertidal habitat-based flood mitigation solutions and barrier-based flood reduction strategies may have adverse effects on flood risk reduction in the lower Thames Estuary. This highlights the importance of fully understanding the varying roles of intertidal habitats across different estuaries and storm conditions to ensure effective and sustainable estuarine flood management strategies.

4.2. Limitations

By disentangling the roles of various frequency bands and their respective responses to habitat presence, our study provides a fundamental understanding of how intertidal habitats influence storm-induced estuarine flooding through modulating different tidal and surge constituents (Section 3.2.5). However, there are several constraints in our semi-analytical approach associated with the various assumptions and simplifications shown in Section 2.1. For instance, the semi-analytical model is linear to enable an explicit calculation of separate tide and surge constituents, while disregarding nonlinear processes, e.g., advection, baroclinic flow (Wei et al., 2017, 2021), and tide-surge interactions (Wei et al., 2019). This may cause deviations of water levels from observations in the upper estuary which is shallower and more frictional with strong nonlinear effects. As shown in Fig. 7, our model underestimates the low water levels by up to 0.6 m at Tilbury and 0.9 m at Silvertown. This underestimation could reduce the modeled storage capacity of intertidal areas during ebb tide, which may lead to an overestimation of the amplitude of water storage fluctuations over these areas, as well as its contribution to the intertidal-subtidal water exchange and its effects on tides and surges in the upper estuary. In addition, the semi-analytical model resolves the 1D intertidal water motion by neglecting the lateral and vertical variability of intertidal variables/parameters, e.g., current velocity, surface gradient, bed slope, bottom friction, which may modulate the intertidal effects on the EWL. Nevertheless, the comparison between the numerical model and semi-analytical model results confirms that habitat-induced changes to

water levels are typically larger than the water level differences between both models in the lower estuary where the water depth is relatively large compared to water level variations (see Fig. 5).

By considering simplified bathymetry and geometry in this study, such as the exponentially convergent estuary width and the fixed intertidal bed slope, our model does not fully capture the complex network of channels, islands, and micro-topographic features of the real Thames Estuary. Nonetheless, the model reproduces the observed tides, surges, and extreme water levels along the Thames Estuary during storm Xaver, indicating that the key physical processes and estuarine features are well represented. The influence of intertidal habitats on flood risks, however, could differ if a different set of estuary or storm parameters were used, as suggested by the effect of the barrier closure and channel depth changes discussed in Sections 3.2.6 and 3.2.7. Also, by assuming a spatially uniform longitudinal wind stress, the lateral wind stress is neglected in the experiments considered in this study. This lateral stress may contribute to the water exchange between the intertidal and subtidal areas and hence affect the intertidal habitat roles in estuarine flooding, e.g., during storm events with strong cross-estuary winds.

This study includes a sensitivity analysis only for channel depth, although other parameters are also important for intertidal effects on estuarine flooding. For example, the roles of intertidal areas may become more significant when considering wider intertidal habitats or when relocating these habitats further landward (Zhu et al., 2025). In addition, water levels are directly forced by tide/surge forcing at the mouth and wind forcing at the surface (Wei et al., 2019), and increases in these forcings could enhance intertidal effects. Moreover, the tide and surge wave propagation along estuaries depends on multiple factors, such as estuary length, width convergence, water depth, bottom friction, bed slope, and long-wave frequency/period (Jay, 1991), all of which can influence how intertidal areas modulate different tide and surge components and extreme high water levels. Given the complexity of intertidal effects, a comprehensive sensitivity study will be conducted in the future by applying our semi-analytical model to different estuaries and storm events, while accounting for various human activities (e.g., reclamation, dredging, damming) and climate change scenarios (e.g., increased extreme weather, sea-level rise). Despite these limitations, our semi-analytical model provides a computationally efficient way to quickly assess the effects of intertidal habitats on estuarine flooding.

5. Conclusions

To investigate the role of intertidal areas in storm-induced flooding and extreme high water levels (EWL) in estuaries, we developed a three-dimensional, idealized semi-analytical tide-surge model that accounts for the interactions between subtidal and intertidal water motions. In this model, tides and surges are calculated separately and decomposed into several major constituents with different frequencies and phases. We found that, in a simple test scenario, the water levels from the semi-analytical model closely match those from the numerical Delft3D model. To understand how intertidal habitats influence various tide and surge components and their roles in flooding in realistic estuaries, we then applied the semi-analytical model to the idealized Thames Estuary (UK) during the storm Xaver, the most severe North Sea surge over the past seven decades, using simplified geometry, bathymetry, and forcing conditions.

Our semi-analytical model reproduces each tide and surge constituent, total water level, and EWL along the Thames Estuary during Xaver in good agreement with observations. Our results show that the predominant semi-diurnal tides and lower-frequency surges (with periods greater than ~24 h) are the main contributors to the high EWL during Xaver, while the higher-frequency tides and surges tend to decrease the EWL. The intertidal effects on water level variations are most pronounced for the semi-diurnal tides and surges, which are amplified along the estuary. These habitats also tend to delay the tide and surge propagation, with the phase delay increasing with frequency. Intertidal effects on the lower-frequency tides and surges in the estuary are minor.

Consequently, because of the existence of intertidal areas, the peak tide and surge height along the Thames Estuary during Xaver are respectively increased by as much as 0.17 m and 0.1 m, while the EWL is elevated by more than 0.1 m. The increase in the EWL results from the habitat-induced change in both the amplitude of semi-diurnal tidal constituents and the phase of semi-diurnal surge components. Our results confirm that the closure of the Thames Barrier during the storm effectively reduces the flooding risk upstream of the storm surge barrier. However, this closure cuts the tidal river and thereby reduces the estuary length, which causes an increase in the EWL by up to 0.2 m around the barrier due to the amplification of tidal and surge wave oscillations. This can cause more severe flood hazards for the outer Thames Estuary. More importantly, intertidal effects on estuarine flooding can shift from increasing to decreasing the EWL as channel depth decreases, because intertidal habitats amplify the dominant tide and surge waves in deeper systems but dampen them in shallower ones. This implies greater effectiveness of intertidal habitats for flood mitigation in the idealized Thames Estuary when it is shallower.

Our study highlights the varying roles of intertidal areas in affecting estuarine flood hazards through modulating different tide and surge constituents. Our findings offer crucial scientific guidance for effective flood mitigation and habitat restoration strategies to mitigate estuarine climate risks in the face of accelerated climate change and intense human activities.

CRediT authorship contribution statement

Renjie Zhu: Writing – review & editing, Writing – original draft, Visualization, Validation, Software, Resources, Methodology, Investigation, Funding acquisition, Formal analysis, Data curation, Conceptualization. **Wei Zhang:** Writing – review & editing, Supervision, Resources, Project administration, Investigation, Funding acquisition, Conceptualization. **Xiaoyan Wei:** Writing – review & editing, Validation, Supervision, Software, Resources, Project administration, Methodology, Investigation, Funding acquisition, Formal analysis, Data curation, Conceptualization.

Declaration of competing interest

The authors declare that they have no known competing financial interests or personal relationships that could have appeared to influence the work reported in this paper.

Acknowledgements

This work was funded by the National Natural Science Foundation of China (NSFC, 42576156, U2040203), the Open Research Fund Program of State Key Laboratory of Water Disaster Prevention (2024491011), the Fundamental Research Funds for the Central Universities (B240205032), the Key Laboratory of Ministry of Education for Coastal Disaster and Protection (J202201), the UK Natural Environment Research Council (CHAMFER project, NE/W004992/1), and the China Scholarship Council (CSC, File 202406710099). XW also acknowledges support from the Royal Society International Exchanges 2022 Cost Share (IEC\NSFC\223066). The authors also appreciate the Port of London Authority who supplied the observed tide/surge, and geometry/bathymetry data of the Thames Estuary.

Appendix A. One-Dimensional Water Motion over Intertidal Habitats

In this section, the water exchange across the intertidal-subtidal interface, the intertidal momentum loss/gain due to bottom friction and surface wind, and the linear assumption of intertidal water level are derived in detail.

By integrating the three-dimensional continuity equation [Eq. (1)] over the cross-section (a triangular area) of the intertidal habitat, combined with the kinematic boundary conditions at the bottom and surface [Eqs. (7) and (9)], the intertidal-subtidal water exchange satisfies

$$\int_{\frac{B}{2}}^{\frac{B_t}{2}}\left[\int_{-h}^{\eta}(\nabla\cdot\mathbf{U})dz\right]dy=\int_{\frac{B}{2}}^{\frac{B_t}{2}}\left(\frac{\partial}{\partial x}\int_{-h}^{\eta}udz+\frac{\partial}{\partial y}\int_{-h}^{\eta}vdz+\frac{\partial\eta}{\partial t}\right)dy$$

$$=\frac{\partial(u_fA_f)}{\partial x}-\underbrace{\int_{-h}^{\eta}\left[-\frac{d}{dx}\left(\frac{B}{2}\right)u+v\right]dz\Big|_{y=\frac{B}{2}}}_{=\alpha F_n}+\int_{\frac{B}{2}}^{\frac{B_t}{2}}\frac{\partial\eta}{\partial t}dy$$

$$=\frac{\partial}{\partial x}\left[u_f\frac{h_fB_f(\eta_f/h_f+1)^2}{4}\right]-\alpha F_n+\frac{B_f(1+\eta_f/h_f)}{2}\frac{\partial\eta_f}{\partial t}=0, \tag{A1}$$

Here, $A_f=h_fB_f(\eta_f/h_f+1)^2/4$ indicates the intertidal area on each side of the cross-section, and $B_t=B+B_f(1+\eta_f/h_f)$ is the time-varying total estuary width including both the intertidal and subtidal regions. The depth-integrated water flux vanishes at shorelines on both sides of the estuary (i.e., at $y=\pm B_t/2$) due to zero total depth. By expanding Eq. (A1) asymptotically in η_f/h_f (which is a small parameter less than unity) and neglecting higher-order terms [e.g., $O(\eta_f/h_f)$, $O\left(\eta_f^2/h_f^2\right)$], the linearized leading-order water exchange F_n is derived in Eq. (10).

Integrating the three-dimensional vertical shear term in Eq. (2) within the intertidal cross-section and implementing the dynamic boundary conditions at the free surface and bottom [Eqs. (7) and (9)] yield the one-dimensional Reynolds stress term M_R

$$M_R=\frac{1}{A_f}\int_{\frac{B}{2}}^{\frac{B_t}{2}}\left[\int_{-h}^{\eta}\frac{\partial}{\partial z}\left(A_v\frac{\partial u}{\partial z}\right)dz\right]dy$$

$$=\frac{1}{A_f}\int_{\frac{B}{2}}^{\frac{B_t}{2}}\left(\frac{\tau_x}{\rho}-su|_{z=-h}\right)dy$$

$$=-\frac{2s_f}{h_f+\eta_f}u_f+\frac{2\tau_x}{(h_f+\eta_f)\rho}. \tag{A2}$$

Here, $s_f=\overline{su|_{z=-h}}/u_f$ (the overbar represents the width average over intertidal habitats) is the intertidal slip parameter measuring the bottom friction averaged within the intertidal cross-section. The first term in Eq. (A2) represents intertidal momentum dissipation due to bottom friction, and the second term measures intertidal momentum gain/loss induced by wind stress, with both terms scaling inversely with the water depth. To enable the semi-analytical approach, the higher-order terms of M_R are neglected by expanding $1/(h_f+\eta_f)$ asymptotically in η_f/h_f, considering only the leading-order term:

$$\frac{1}{(h_f+\eta_f)}=\frac{1}{h_f}\left[1-\frac{\eta_f}{h_f}+O\left(\frac{\eta_f^2}{h_f^2}\right)\right]\approx\frac{1}{h_f}. \tag{A3}$$

By substituting Eq. (A3) into Eq. (A2), the linearized leading-order M_R is derived in Eq. (11).

The relationship between the laterally averaged intertidal water level (η_f) and the subtidal water level (η) is derived based on the linear assumption mentioned in Section 2.1.2:

$$\eta_f=(\eta+h_f)\sqrt{\frac{2h_f/B_f}{2h_f/B_f-\mathrm{sign}(y)\eta_y}}-h_f,\ \text{at } y=\pm\frac{B(x)}{2}. \tag{A4}$$

Here, we assume the intertidal bed slope $2h_f/B_f$ ($\sim10^{-3}$) is much greater than the lateral surface gradient η_y ($\sim10^{-5}$). An asymptotic expansion can be applied to the square root term in Eq. (A4) with respect to $\eta_y/(2h_f/B_f)$ ($\ll1$),

$$\eta_f = \eta + \frac{\mathrm{sign}(y)\eta_y B_f}{4}\left(\frac{\eta}{h_f}+1\right) + O\left[\frac{\eta_y^2}{(2h_f/B_f)^2}\right] \approx \eta + \frac{\mathrm{sign}(y)\eta_y}{4}B_f, \tag{A5}$$

with nonlinear terms of higher orders neglected, thereby establishing the linearized leading-order relationship between η_f and η in Eq. (12).

Appendix B. Semi-Analytical Model Approach

In the semi-analytical model, any water flux integrated from $z = 0$ to $z = \eta$, e.g., in Eqs. (5) and (6), is neglected due to its higher order as the nonlinear Stokes drift (Kumar et al., 2017). According to Chen et al. (2016), the current velocity in the subtidal region can be analytically expressed as functions of sea surface gradients by substituting Eq. (13) into Eqs. (2) and (3) for each tide and surge component,

$$\int_{-h}^{0}\left(\widehat{u}_{T_j},\widehat{v}_{T_j}\right)dz = \mathbf{D}\left(\sigma_{T_j}\right)\nabla\widehat{\eta}_{T_j}, \text{ and } \int_{-h}^{0}\left(\widehat{u}_{S_k},\widehat{v}_{S_k}\right)dz = \mathbf{D}\left(\sigma_{S_k}\right)\nabla\widehat{\eta}_{S_k} + \mathbf{F}_{S_k}. \tag{B1}$$

Here, the matrix $\mathbf{D}$ is a function of the frequency σ

$$\mathbf{D}(\sigma) = -\frac{gh}{2i\sigma}\begin{bmatrix} C^+ + C^- & i(C^+ - C^-) \\ -i(C^+ - C^-) & C^+ + C^- \end{bmatrix}, \tag{B2}$$

with

$$C^{\pm}(\sigma) = \frac{1}{1 \pm f/\sigma}\left(1 - \alpha_{\pm}\frac{\sinh\delta_{\pm}}{\delta_{\pm}}\right), \tag{B3a}$$

$$\alpha_{\pm} = \left(\cosh\delta_{\pm} + i\frac{1 \pm f/\sigma}{s^*}\frac{\sinh\delta_{\pm}}{\delta_{\pm}}\right)^{-1}, \tag{B3b}$$

$$\delta_{\pm} = \frac{1+i}{\mathrm{Stk}_{\pm}}, \tag{B3c}$$

$$\mathrm{Stk}_{\pm} = \frac{\sqrt{2A_v/(\sigma \pm f)}}{h}. \tag{B3d}$$

Here, $s^* = s/\sigma h$ is the dimensionless subtidal slip parameter, and the term $\mathrm{Stk}_{\pm}$ is the Stokes number, defined as the ratio of the boundary layer thickness to the water depth (Souza, 2013), which measures the effect of bottom layer turbulence on the vertical structure of velocity and density. The term $\mathbf{F}_{S_k}$ is the forcing vector due to wind stress and also determined by the surge frequency,

$$\mathbf{F}_{S_k} = \frac{1}{2i\sigma_{S_k}\rho}\begin{bmatrix} \tau_k^+ & \tau_k^- \\ -i\tau_k^+ & i\tau_k^- \end{bmatrix}\begin{bmatrix} C_w^+ \\ C_w^- \end{bmatrix}, \tag{B4}$$

with the wind stress coefficients

$$C_w^{\pm}(\sigma_{S_k}) = \frac{1 - \alpha_{\pm}}{1 \pm f/\sigma_{S_k}}. \tag{B5}$$

Here, $\tau_k^{\pm} = \widehat{\tau}_{x_k} \pm i\widehat{\tau}_{y_k}$ is the rotating wind forcing amplitudes, see details in Chen et al. (2016).

In the intertidal region, the current velocity can also be analytically expressed through the derivatives of the intertidal water level by substituting Eq. (13) into Eq. (11) for each tide and surge component,

$$\widehat{u}_{f_{T_j}} = -\frac{g}{i\sigma}C_f\left(\sigma_{T_j}\right)\frac{d\widehat{\eta}_{f_{T_j}}}{dx}, \text{ and } \widehat{u}_{f_{S_k}} = -\frac{g}{i\sigma}C_f\left(\sigma_{S_k}\right)\frac{d\widehat{\eta}_{f_{S_k}}}{dx} + \frac{2\widehat{\tau}_{x_k}}{i\sigma\rho h_f}C_f\left(\sigma_{S_k}\right), \tag{B6}$$

with the coefficient C_f dependent on the frequency σ

$$C_f(\sigma) = \frac{1}{1 - is_f^*}. \tag{B7}$$

Here, $s_f^* = 2s_f/\sigma h_f$ is the dimensionless intertidal slip parameter. Also, the intertidal-subtidal water exchange for each tide and surge component becomes

$$\widehat{F}_n(\sigma) = \frac{1}{\alpha}\frac{d}{dx}\left(\widehat{u}_f\frac{h_f B_f}{4}\right) + \frac{B_f}{2\alpha} i\sigma\widehat{\eta}_f, \tag{B8}$$

where $\widehat{F}_n$ includes the contributions from tides ($\widehat{\eta}_{f_{T_j}}$ and $\widehat{u}_{f_{T_j}}$ with $\sigma = \sigma_{T_j}$) and surges ($\widehat{\eta}_{f_{S_k}}$ and $\widehat{u}_{f_{S_k}}$ with $\sigma = \sigma_{S_k}$), respectively.

By integrating Eq. (1) from $z = -h$ to $z = 0$ and applying Eqs. (13) and (B1), the governing equation of the free surface elevation within the subtidal area for each tide and surge component reads,

$$\nabla\cdot\left[\mathbf{D}\left(\sigma_{T_j}\right)\nabla\widehat{\eta}_{T_j}\right] + i\sigma_{T_j}\widehat{\eta}_{T_j} = 0, \text{ and } \nabla\cdot\left[\mathbf{D}\left(\sigma_{S_k}\right)\nabla\widehat{\eta}_{S_k}\right] + i\sigma_{S_k}\widehat{\eta}_{S_k} = -\nabla\cdot\mathbf{F}_{S_k}, \tag{B9}$$

with the corresponding boundary conditions

$$\widehat{\eta}_{T_j} = A_{T_j},\ \widehat{\eta}_{S_k} = A_{S_k},\ \text{at } \partial_S\Omega, \tag{B10a}$$

$$\left[\mathbf{D}\left(\sigma_{T_j}\right)\nabla\widehat{\eta}_{T_j}\right]\cdot\mathbf{n}_\mathrm{h} = \widehat{F}_n\left(\sigma_{T_j}\right),\ \left[\mathbf{D}\left(\sigma_{S_k}\right)\nabla\widehat{\eta}_{S_k} + \mathbf{F}_{S_k}\right]\cdot\mathbf{n}_\mathrm{h} = \widehat{F}_n\left(\sigma_{S_k}\right),\ \text{at } \partial_F\Omega, \tag{B10b}$$

$$\left[\mathbf{D}\left(\sigma_{T_j}\right)\nabla\widehat{\eta}_{T_j}\right]\cdot\mathbf{n}_\mathrm{h} = \left[\mathbf{D}\left(\sigma_{S_k}\right)\nabla\widehat{\eta}_{S_k} + \mathbf{F}_{S_k}\right]\cdot\mathbf{n}_\mathrm{h} = 0, \text{at } \partial_R\Omega. \tag{B10c}$$

Eq. (B10b) shows that the intertidal habitat affects estuarine tides and surges by the exchange F_n between intertidal and subtidal areas. The two-dimensional linear elliptic partial differential equation [Eq. (B9)] can be numerically solved using the finite element method (Gockenbach, 2006), combined with the boundary conditions [Equation (B10)]. More details of the numerical procedure can be found in Kumar et al. (2016) and Zhu et al. (2025).

Appendix C. Observed Water Level and Wind Velocity Data

The total water level at the upstream three gauges (Fig. C1), the performance of the tide and surge decomposition (Fig. C2), the wind field in the North Sea and the Thames Estuary (Fig. C3), and the time series of the longitudinal and lateral wind speed on four different sites along the Thames Estuary (Fig. C4) are shown in this section.

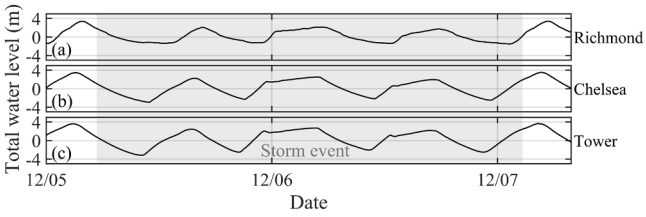

Fig. C1. Time series of the sea surface elevation during storm Xaver in tide gauges (a)-(c) from Richmond near the tidal limit to Tower upstream of the Thames Barrier. The gray box denotes the period during which the storm Xaver occurred.

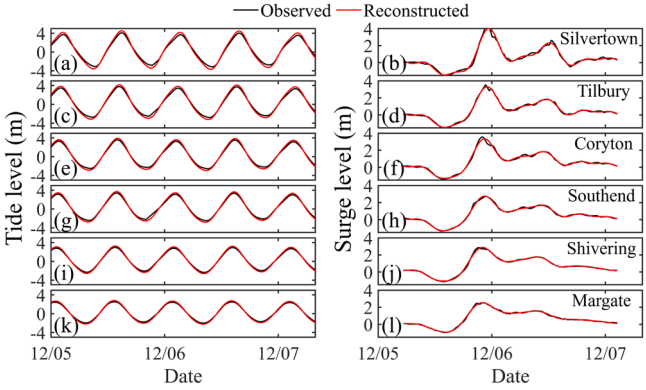

Fig. C2. Observed (black lines) and reconstructed (red lines) water level induced by tides (left column) and surges (right column) in tide gauges from Silvertown (first row) near the Thames Barrier to Margate (last row) at the mouth. The reconstructed tidal elevation is calculated by T_TIDE harmonic analysis (Pawlowicz et al., 2002), while the reconstructed surge elevation is calculated by the fast Fourier transform with a low-pass filter (Spicer et al., 2019).

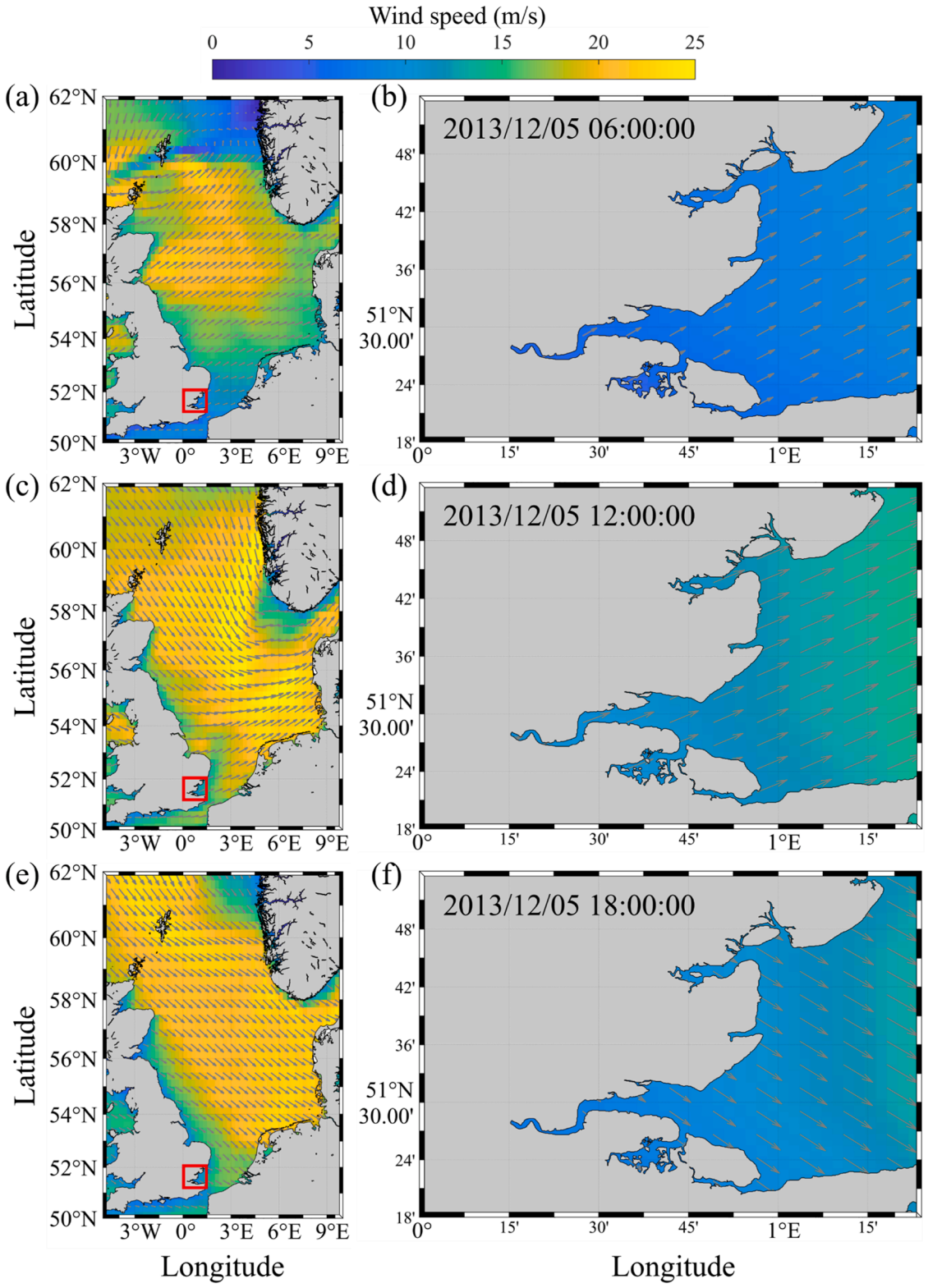

Fig. C3. Wind velocities in the North Sea (left column) and the Thames Estuary (right column) at three moments during the storm Xaver on December 5, 2013—6:00 (first row), 12:00 (second row), and 18:00 (third row)—when the wind within the estuary was relatively strong. The red boxes mark the study area, i.e., the Thames Estuary. The colors and arrows show the magnitude and direction of the wind velocity.

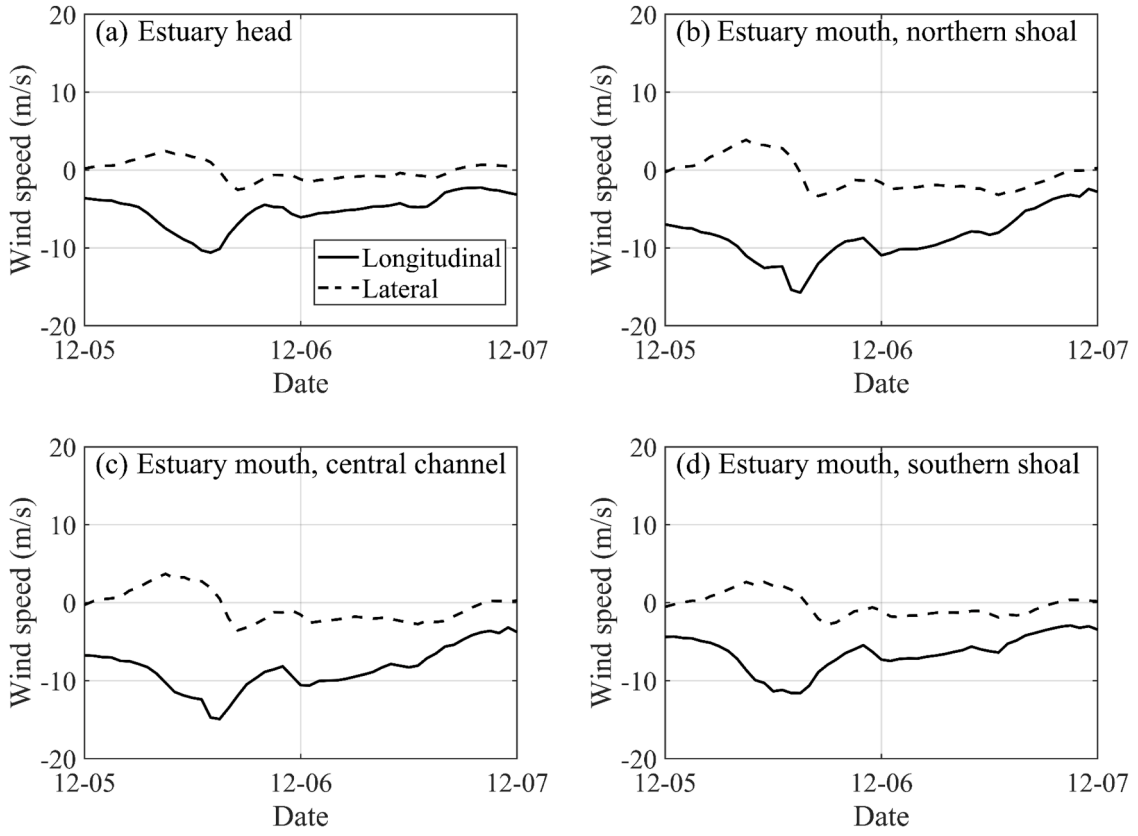

Fig. C4. Longitudinal (solid line) and lateral (dashed line) wind velocities during the storm Xaver on four sites of the Thames Estuary: (a) the estuary head (0.3°W, 51.4°N), (b) the northern shoal (1.4°W, 51.8°N), (c) the central channel (1.4°W, 51.6°N), and (d) the southern shoal (1.4°W, 51.4°N) of the estuary mouth.

Appendix D. Model Comparison

Table D1
Computational performance comparison between the semi-analytical model and the numerical Delft3D model on a 6-core CPU.

Model features & computational characteristics	Semi-analytical model	Numerical Delft3D model
Mesh type	Triangle	Rectangle
Horizontal nodes	54,751	14,000
Vertical layers	30	10
Computation time	1 min	30 min
Memory usage	2 MB	3 GB

Appendix E. External and Internal Surge Forcing

The different contributions of externally forced and internally wind-induced surges (Fig. E1) are shown in this section.

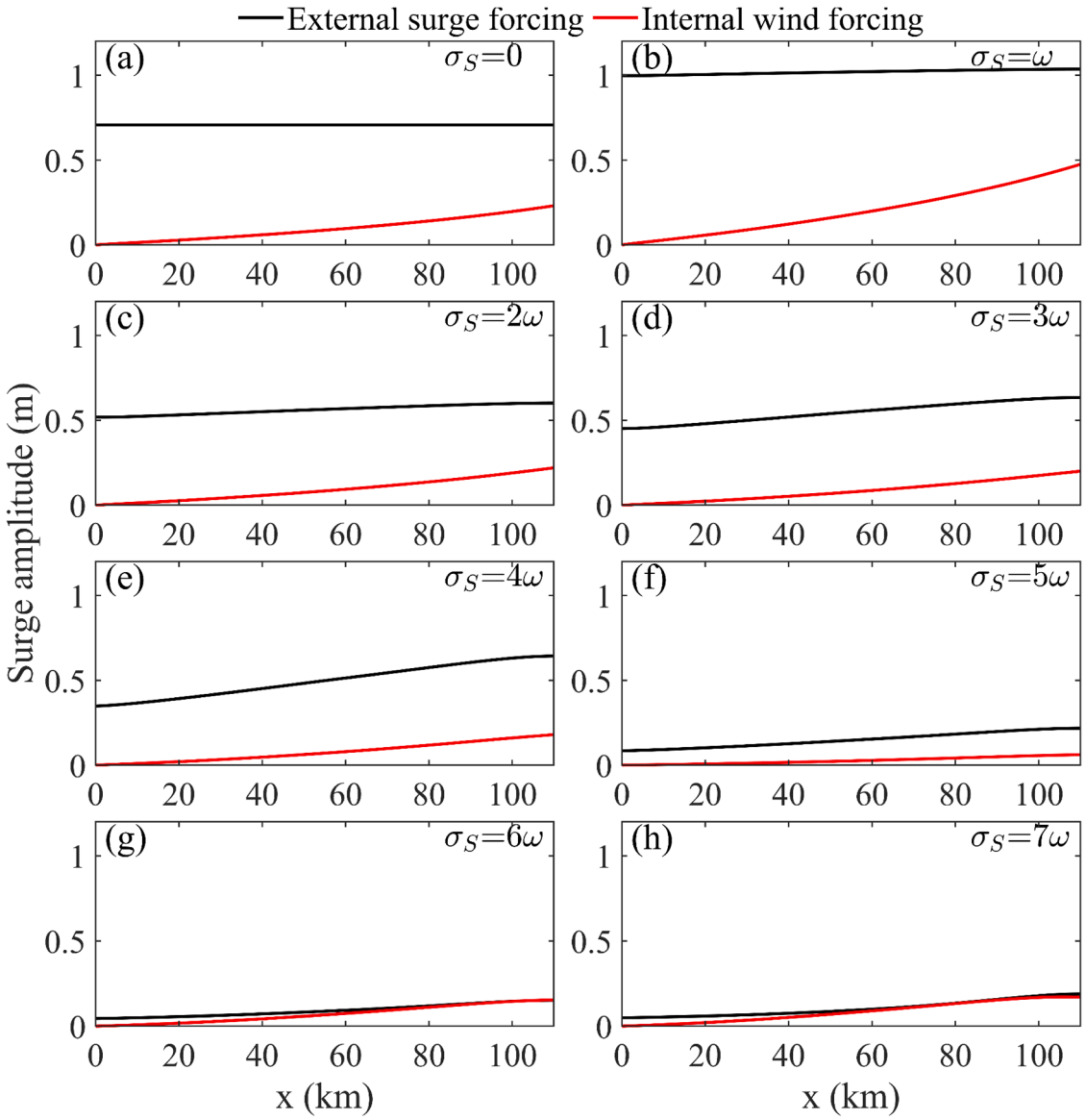

Fig. E1. Amplitude of the externally forced surge (black lines) and the internally wind-induced surge (red lines) for different components (a)-(h) with the surge frequency σ_S varying from 0 to 7ω.

Data availability

The code for the semi-analytical model and the data that support the findings of this study are available on Zenodo (https://doi.org/10.5281/zenodo.17682398).

References

ABP Marine Environmental Research Ltd., 2013. Hub for London. Ecology Desk Study. Part B: Marine and Coastal Baseline. ABPmer Report No. R.2130. August 2013.
Arns, A., Wahl, T., Dangendorf, S., Jensen, J., 2015. The impact of sea level rise on storm surge water levels in the northern part of the German Bight. Coast. Eng. 96, 118–131.
Barbier, E.B., et al., 2011. The value of estuarine and coastal ecosystem services. Ecol. Monogr. 81 (2), 169–193.
Burningham, H., French, J., 2011. Seabed dynamics in a lage coastal embayment: 180 years of morphological change in the outer Thames estuary. Hydrobiologia 672 (1), 105–119.
Chen, W.L., et al., 2016. Response of large-scale coastal basins to wind forcing: influence of topography. Ocean. Dyn. 66 (4), 549–565.
Deltares, 2025. Delft3D-flow hydro-morphodynamics user manual. Deltares, accessed 8 July 2025. https://oss.deltares.nl/web/delft3d/.
Doody, J.P., 2004. 'Coastal squeeze' – an historical perspective. J. Coast. Conserv. 10 (1), 129.
Dykstra, S.L., Talke, S.A., Yankovsky, A.E., Torres, R., Viparelli, E., 2024. Reflection of storm surge and tides in convergent estuaries with dams, the case of Charleston, USA. J. Geophys. Res.: Oceans 129 (9).
Familkhalili, R., Talke, S.A., Jay, D.A., 2020. Tide-storm surge interactions in highly altered estuaries: how channel deepening increases surge vulnerability. J. Geophys. Res.: Oceans 125 (4).
Friedrichs, C.T., Aubrey, D.G., 1994. Tidal propagation in strongly convergent channels. J. Geophys. Res 99 (C2), 3321.
Gockenbach, M.S., 2006. Understanding And Implementing the Finite Element Method. Society for Industrial and Applied Mathematics, USA, p. 363.
Gou, X., et al., 2023. The Impact of coastline and bathymetry changes on the storm tides in Zhejiang Coasts. J. Mar. Sci. Eng. 11 (9), 1832.
Grant, A., Cooker, M.J., 2023. Reductions in water level over coastal wetlands during storm surges and tsunamis: an analytical result and a critical review of the literature. Coast. Eng. 183, 104328.

Grigg, M., Cucknell, A., Marten, K., Cox, T., Yesson, C., 2025. Habitat suitability modelling for restoration of intertidal seagrass, Zostera noltei: a case study from the Greater Thames Estuary, UK. Estuar. Coast. Shelf. Sci. 312, 109039.
Guo, L., et al., 2022. Reclamation of tidal flats within tidal basins alters centennial morphodynamic adaptation to sea-level rise. J. Geophys. Res.: Earth Surf. 127 (6), e2021JF006556.
Hersbach, H., et al., 2020. The ERA5 global reanalysis. Q. J. R. Meteorol. Soc. 146 (730), 1999–2049.
Hu, K., Chen, Q., Wang, H., 2015. A numerical study of vegetation impact on reducing storm surge by wetlands in a semi-enclosed estuary. Coast. Eng. 95, 66–76.
Jalón Rojas, I., et al., 2021. Multidecadal evolution of the turbidity maximum zone in a macrotidal river under climate and anthropogenic pressures. J. Geophys. Res.: Oceans 126 (5).
Jay, D.A., 1991. Green's law revisited: tidal long-wave propagation in channels with strong topography. J. Geophys. Res 96 (C11), 20585.
Kettle, A.J., 2020. Storm Xaver over Europe in December 2013: overview of energy impacts and North Sea events. Adv. Geosci. 54, 137–147.
Kiesel, J., MacPherson, L.R., Schuerch, M., Vafeidis, A.T., 2022. Can Managed realignment buffer extreme surges? the relationship between marsh width, vegetation cover and surge attenuation. Estuaries Coasts 45 (2), 345–362.
Kumar, M., Schuttelaars, H.M., Roos, P.C., 2017. Three-dimensional semi-idealized model for estuarine turbidity maxima in tidally dominated estuaries. Ocean Model. 113, 1–21.
Kumar, M., Schuttelaars, H.M., Roos, P.C., Möller, M., 2016. Three-dimensional semi-idealized model for tidal motion in tidal estuaries. Ocean. Dyn. 66 (1), 99–118.
Lavery, S., Donovan, B., 2005. Flood risk management in the Thames Estuary looking ahead 100 years. Philos. Trans. R. Soc. A: Math. Phys. Eng. Sci. 363 (1831), 1455–1474.
Li, C., et al., 2016. Influence of retention basins on tidal dynamics in estuaries: application to the Ems estuary. Ocean. Coast. Manage 134, 216–225.
Loder, N.M., Irish, J.L., Cialone, M.A., Wamsley, T.V., 2009. Sensitivity of hurricane surge to morphological parameters of coastal wetlands. Estuar. Coast. Shelf. Sci. 84 (4), 625–636.
Lorentz, H.A., 1926. Verslag Staatscommissie Zuiderzee 1918-1926. Algemeene Landsdrukkerij, p. 345.
Marsooli, R., Orton, P.M., Georgas, N., Blumberg, A.F., 2016. Three-dimensional hydrodynamic modeling of coastal flood mitigation by wetlands. Coast. Eng. 111, 83–94.
Mikhailov, V.N., Mikhailova, M.V., 2012. Tides and storm surges in the Thames River Estuary. Water Resour. 39 (4), 351–365.
Möller, I., et al., 2014. Wave attenuation over coastal salt marshes under storm surge conditions. Nat. Geosci. 7 (10), 727–731.
Moraes, R.P.L., Reguero, B.G., Mazarrasa, I., Ricker, M., Juanes, J.A., 2022. Nature-Based Solutions in Coastal and Estuarine Areas of Europe. Front. Environ. Sci. 10.
Murray, N.J., et al., 2019. The global distribution and trajectory of tidal flats. Nature 565 (7738), 222–225.
Musgrove, A.J., Langston, R.H.W., Baker, H., Ward, R.M, 2003. Estuarine waterbirds at low tide: the WeBS low tide counts 1992–93 to 1998–99. WSG/BTO/WWT/RSPB/JNCC. Thetford.
Nidzieko, N.J., Ralston, D.K., 2012. Tidal asymmetry and velocity skew over tidal flats and shallow channels within a macrotidal river delta. J. Geophys. Res.: Oceans 117 (C3), C03001.
O'Reilly-Wiese, S.B., MacLeod, C.L., Lester, J.N., 1997. A recent history of metal accumulation in the sediments of the Thames Estuary. U. K., Estuaries 20 (3), 483–493.
Orton, P., et al., 2015. Channel Shallowing as Mitigation of Coastal Flooding. J. Mar. Sci. Eng. 3 (3), 654–673.
Pawlowicz, R., Beardsley, B., Lentz, S., 2002. Classical tidal harmonic analysis including error estimates in MATLAB using T_TIDE. Comput. Geosci. 28 (8), 929–937.
Proudman, J., 1955. The propagation of tide and surge in an estuary. Proc. R. Soc. L. Math. Phys. Sci. 231 (1184), 8–24.
Reed, D., van Wesenbeeck, B., Herman, P.M.J., Meselhe, E., 2018. Tidal flat-wetland systems as flood defenses: understanding biogeomorphic controls. Estuar. Coast. Shelf. Sci. 213, 269–282.
Reef, K.R.G., Lipari, G., Roos, P.C., Hulscher, S.J.M.H., 2018. Time-varying storm surges on Lorentz's Wadden Sea networks. Ocean. Dyn. 68 (8), 1051–1065.
Restemeyer, B., van den Brink, M., Woltjer, J., 2018. Resilience unpacked - framing of 'uncertainty' and 'adaptability' in long-term flood risk management strategies for London and Rotterdam. Eur. Plan. Stud. 26 (8), 1559–1579.
Restemeyer, B., Van Den Brink, M., Woltjer, J., 2019. Decentralized implementation of flood resilience measures - a blessing or a curse? lessons from the Thames Estuary 2100 Plan and the Royal Docks regeneration. Plan. Pract. Res. 34 (1), 62–83.
Richardson, M., Soloviev, M., 2021. The Thames: arresting Ecosystem decline and building back better. Sustainability 13 (11), 6045.
Rossington, K., Spearman, J., 2009. Past and future evolution in the Thames Estuary. Ocean. Dyn. 59 (5), 709–718.
Schramkowski, G.P., de Swart, H.E., 2002. Morphodynamic equilibrium in straight tidal channels: combined effects of the Coriolis force and external overtides. J. Geophys. Res.: Oceans 107 (C12), 20-1-20-17.
Schuttelaars, H.M., de Jonge, V.N., Chernetsky, A., 2013. Improving the predictive power when modelling physical effects of human interventions in estuarine systems. Ocean. Coast. Manage 79, 70–82.
Shen, Y., Jia, H., Li, C., Tang, J., 2018. Numerical simulation of saltwater intrusion and storm surge effects of reclamation in Pearl River Estuary, China. Appl. ocean res. 79, 101–112.
Smolders, S., Plancke, Y., Ides, S., Meire, P., Temmerman, S., 2015. Role of intertidal wetlands for tidal and storm tide attenuation along a confined estuary: a model study. Nat. Hazards Earth Syst. Sci. 15 (7), 1659–1675.
Song, H., et al., 2020. Nonlinear tide-surge-wave interaction at a shallow coast with large scale sequential harbor constructions. Estuar. Coast. Shelf. Sci. 233, 106543.
Soulsby, R., 1997. Dynamics of Marine Sands. A Manual for Practical Applications. Thomas Telford, London, UK.
Souza, A.J., 2013. On the use of the Stokes number to explain frictional tidal dynamics and water column structure in shelf seas. Ocean Sci. 9 (2), 391–398.
Spencer, T., Brooks, S.M., Evans, B.R., Tempest, J.A., Möller, I., 2015. Southern North Sea storm surge event of 5 December 2013: water levels, waves and coastal impacts. Earth-Sci. Rev. 146, 120–145.
Spicer, P., Huguenard, K., Ross, L., Rickard, L.N., 2019. High-frequency tide-surge-river interaction in Estuaries: causes and implications for coastal flooding. J. Geophys. Res.: Oceans 124 (12), 9517–9530.
Stark, J., Plancke, Y., Ides, S., Meire, P., Temmerman, S., 2016. Coastal flood protection by a combined nature-based and engineering approach: modeling the effects of marsh geometry and surrounding dikes. Estuar. Coast. Shelf Sci. 175, 34–45.
Stark, J., Smolders, S., Meire, P., Temmerman, S., 2017. Impact of intertidal area characteristics on estuarine tidal hydrodynamics: a modelling study for the Scheldt Estuary. Estuar. Coast. Shelf Sci. 198, 138–155.
Talke, S.A., Jay, D.A., 2020. Changing tides: the role of natural and anthropogenic factors. Ann. Rev. Mar. Sci. 12, 121–151.
Talke, S.A., Familkhalili, R., Jay, D.A., 2021. The influence of channel deepening on tides, river discharge effects, and storm surge. J. Geophys. Res.: Oceans 126 (5).
Townend, I., Pethick, J., 2002. Estuarine flooding and managed retreat. Philos. Trans. R. Soc. Lond., A: Math. Phys. Eng. Sci. 360 (1796), 1477–1495.
Tye, A.M., Rushton, J., Vane, C.H., 2018. Distribution and speciation of phosphorus in foreshore sediments of the Thames estuary, UK. Mar, Pollut, Bull 127, 182–197.
UK Centre for Ecology & Hydrology, 2025. Natl. River Flow Arch. Available at: https://nrfa.ceh.ac.uk/.
Wadey, M.P., et al., 2015. A comparison of the 31 January–1 February 1953 and 5–6 December 2013 coastal flood events around the UK. Front. Mar. Sci. 2.
Wamsley, T.V., Cialone, M.A., Smith, J.M., Atkinson, J.H., Rosati, J.D., 2010. The potential of wetlands in reducing storm surge. Ocean Eng. 37 (1), 59–68.
Wei, X., et al., 2019. Impact of storm propagation speed on coastal flood hazard induced by offshore storms in the North Sea. Ocean Model. 143, 101472.
Wei, X., et al., 2021. Unraveling interactions between asymmetric tidal turbulence, residual circulation, and salinity dynamics in short, periodically weakly stratified estuaries. J Phys Ocean. 51 (5), 1395–1416.
Wei, X., Kumar, M., Schuttelaars, H.M., 2017. Three-dimensional salt dynamics in well-mixed estuaries: influence of estuarine convergence, coriolis, and bathymetry. J Phys Ocean. 47 (7), 1843–1871.
Wei, X., Kumar, M., Schuttelaars, H.M., 2018. Three-dimensional sediment dynamics in well-mixed estuaries: importance of the internally generated overtide, spatial settling lag, and gravitational circulation. J. Geophys. Res.: Oceans 123 (2), 1062–1090.
Wei, X., Schramkowski, G.P., Schuttelaars, H.M., 2016. Salt Dynamics in Well-Mixed Estuaries: importance of Advection by Tides. J. Phys. Ocean 46 (5), 1457–1475.
Williams, J., O'Neill, C., 2024. Atlas of Tides, North West European Shelf. Volume II: Tide and Surge. National Oceanography Centre, Southampton.
Willmott, C.J., 1981. On the validation of models. Phys. Geogr. 2 (2), 184–194.
Winant, C.D., 2007. Three-dimensional tidal flow in an elongated, rotating basin. J. Phys. Ocean. 37 (9), 2345–2362.
Zhang, H., Shen, Y., Tang, J., 2023. Wave and storm surge evolutions in the Pearl River Estuary with large-scale land reclamation impacts. Ocean. Eng. 273, 113977.
Zhang, M., et al., 2021. Tidal-flat reclamation aggravates potential risk from storm impacts. Coast. Eng. 166, 103868.
Zhu, R., Zhang, W., Wei, X., 2025. Impact of intertidal habitats on hydrodynamics in tidally energetic, well-mixed Estuaries. J. Phys. Ocean 55 (8), 1155–1191.